UNIVERSITY OF CALIFORNIA

Los Angeles

Broadband Nonreciprocal RF Front-Ends Based on Time-Varying Transmission Lines

A dissertation submitted in partial satisfaction

of the requirements for the degree

Doctor of Philosophy in Electrical Engineering

by

Shihan Qin

2016

© Copyright by
Shihan Qin
2016

ABSTRACT OF THE DISSERTATION

Broadband Nonreciprocal RF Front-Ends Based on Time-Varying Transmission Lines

by

Shihan Qin

Doctor of Philosophy in Electrical Engineering

University of California, Los Angeles, 2016

Professor Yuanxun Wang, Chair

Nonreciprocal components like circulators are often used to separate transmitting and receiving signals sharing a common antenna such as those in the front-end of a monostatic continuous-wave radar or a full-duplex radio that performs simultaneous transmit and receive (STAR) over the same frequency band. In those systems, the isolation of the circulator is critical in preventing the receiver from being interfered or jammed by the transmitted signal. Classical ferrite circulators are essentially cavities supporting non-reciprocal resonant modes. They are intrinsically narrowband, bulky, and hard to be integrated on modern integrated circuits (ICs). In comparison, active circulators have been developed based on the nonreciprocal transfer characteristics of transistors. They offer small physical dimensions, versatile functionalities, and compatibility with IC technology. However, active circulators have generally limited noise and power performances which prevent them from being widely deployed in systems requiring wide dynamic ranges.

Time-varying transmission lines (TVTL) such as Distributedly Modulated Capacitors (DMC) are transmission lines loaded with varactors whose capacitances are modulated by a unidirectionally propagating wave. They translate the direction difference of waves propagating on it into the difference in frequency based on its unidirectional frequency conversion property. In such way, TVTL can behave as a circulator and exhibit broadband isolation

due to the non-resonant nature of the traveling wave structure. Positive-dB parametric gain may be realized during the frequency conversion process which helps to compensate for the circuit loss.

In this work, a complete theory, based on (1) the distributed parametric effect on a TVTL and (2) the distributed capacitive mixers, is presented with emphasis on the theoretical bounds of the isolation and gain performances of the DMC. The DMCs implemented on Rogers PCB and on GaN MMIC are both presented with the measured results agreeing well with the theoretical derivations and the simulation results. Especially, the MMIC DMC has demonstrated experimentally verified positive-dB receiving (RX) gain and > 10 dB transmitting-versus-receiving (TX/RX) isolation over $0.7 - 2.5$ GHz. Furthermore, a circulator prototype combining a pair of MMIC DMC units in a balanced architecture is assembled and tested. The balanced architecture offers a new level of isolation in addition to what is offered by a single DMC. More than 25 dB TX/RX isolation and less than 2 dB RX loss have been experimentally observed for almost one octave at $0.95 - 1.8$ GHz.

The dissertation of Shihan Qin is approved.

Tatsuo Itoh

Mona Jarrahi

Troy Carter

Yuanxun Wang, Committee Chair

University of California, Los Angeles

2016

Table of Contents

1 Introduction **1**

1.1 Challenges in Wireless Systems 1

1.1.1 Half-Duplex v.s. Full-Duplex 2

1.1.2 Bistatic (Separate-Antenna) v.s. Monostatic (Shared-Antenna) 3

1.2 Circulators for Monostatic Full-Duplex 4

1.2.1 Ferrite Circulators 5

1.2.2 Active Circulators 5

1.2.3 Recent Advances 6

1.3 Circulators Based on TVTL and DMC 6

1.4 Dissertation Outline 8

2 Basics: TVTL and DMC **10**

2.1 Transmission Line with Time-Varying Capacitance 10

2.2 Distributedly Modulated Capacitors as a Circulator 13

2.2.1 Isolation of Finite-Length DMC 15

2.2.2 Conversion Gain of Finite-Length DMC 20

2.2.3 Noise Performance of Finite-Length DMC 22

2.2.4 Power/Linearity Performance of Finite-Length DMC 24

3 Practical DMC Designs **26**

3.1 DMC Design on PCB 26

3.1.1 Simulated Performances 27

3.1.2 Experimental Results 30

3.2 DMC Design on MMIC 37
3.2.1 Linear S-Parameter Test 38
3.2.2 Nonlinear Frequency-Conversion Test – Circulator Performance . . . 40

4 Isolation Improvement – Balanced DMC 44
4.1 Principles 44
4.2 Implementation and Measured Results 47

5 Conclusion 56

A Derivation of the TVTL Solution 58

B General Isolation of Dispersive DMC 62

References 64

List of Figures

1.1 Two types of wireless communications: (a) half-duplex; (b) full-duplex. . . . 2

1.2 The duplexer in a shared-antenna transceiver front-end. 3

1.3 (a) A three-port circulator. (b) A circulator in a transceiver front-end. . . . 4

2.1 Time-varying transmission line where the capacitance per unit length is a function of time and space. 10

2.2 Concept of the proposed DMC for circulator application. 14

3.1 DMC implemented in double-balanced fashion. (a) Transmission-line realization with two units shown. (b) Microstrip-line implementation with one unit shown. 26

3.2 Dispersion behavior of the designed periodically loaded transmission line. . . 28

3.3 Comparison of TX/RX isolation at the sideband $\omega_m - \omega_s$, using uniform and nonuniform capacitance modulations in the DMC. 28

3.4 Simulated noise figure and conversion gain of the receiving signal at the sideband $\omega_m - \omega_s$ through the DMC. 30

3.5 Simulated power/linearity performance of the receiving signal at the sideband $\omega_m - \omega_s$ and the transmitting signal at ω_s through the DMC. 31

3.6 Photo of the DMC prototype on Rogers PCB with 16 units of double-balanced varactor diodes loaded on the microstrip lines. 31

3.7 C-V curve of the MA46580 varactor. 32

3.8 Measurement setup for the isolation and conversion gain performances of the DMC. (a) Photograph. (b) Diagram. 34

3.9 Measured TX/RX isolation in comparison with the simulation and analytical results for the sideband of $\omega_m - \omega_s$. 35

3.10 Measured TX insertion gain defined at the output to the antenna over the input from the transceiver at the original signal frequency. 36

3.11 Measured RX conversion gain defined as the up-converted received signal output to the transceiver at $\omega_m - \omega_s$ over the original input from the antenna at ω_s. 36

3.12 (a) Photo and (b) illustration of the DMC MMIC realized on 0.25 um GaN process. 24 GaN Schottky diodes are in shunt of the meandered microstrip line. 38

3.13 Measured and simulated 2-port small-signal S parameters of the DMC MMIC without carrier pump but with varactor diodes biased at (a) 4.5 V; (b) 5.5 V. 39

3.14 Measurement setup for the circulator performance test of the DMC MMIC. . 40

3.15 Measured and simulated circulator performance of the DMC MMIC at (a) 4.5 V bias of the varactors and 21.4 dBm carrier power; (b) 5.5 V bias of the varactors and 24.8 dBm carrier power. The upper sideband $\omega_m + \omega_s$ is used for RX output. 42

4.1 Block diagram of a balanced combo of two DMCs: the RX port is assigned at a different port of the 90° hybrid from TX. 45

4.2 Block diagram of an alternative balanced DMC: the RX port is assigned at the same port of the 90° hybrid as TX until separated by the diplexer. . . . 47

4.3 The balanced DMC prototype: (a) circuit diagram; (b) top view of the module; (c) bottom view of the module. The size of the fabricated prototype is compared with that of a U.S. penny. 48

4.4 Measured 2-port small-signal S parameters of the balanced DMC module with varactors biased at (a) 4.5 V; (b) 5.5 V. 50

4.5 Measured circulator performance of the balanced DMC at (a) 4.5 V bias of the varactors and 21.4 dBm carrier power; (b) 5.5 V bias of the varactors and 24.8 dBm carrier power. The upper sideband $\omega_m + \omega_s$ is used for RX output. 51

4.6 Measured circulator performance of the balanced DMC at (a) 4.5 V bias of the varactors and 21.4 dBm carrier power; (b) 5.5 V bias of the varactors and 24.8 dBm carrier power. The upper sideband $\omega_m + \omega_s$ is used for RX output. 53

List of Tables

3.1 List of the instruments and the components involved in the measurement setup for the DMC. 33

4.1 List of COTS components used in the balanced DMC module in Fig. 4.3a. . 49

4.2 Summary of the measured performance of the balanced DMC module. 54

ACKNOWLEDGMENTS

I would like to thank my advisor, Professor Yuanxun (Ethan) Wang, for his guidance and support throughout my graduate study at UCLA. Without his knowledge and time, this research work would not have been possible. I am also grateful to Dr. Qiang (Mark) Xu for his many helpful discussions with me on this subject and to Dr. Minji Zhu for his knowledge and instruction in circuit fabrication and measurement performing. In addition, I would like to express my gratitude to my lab peers, including Yonghoon Song, Rui Zhu, Zhi (Jackie) Yao, and Matthew Biedka, for their providing friendly environment in our lab. I would miss all of you and my time spent in our lab because of you.

I am also grateful to my committee members, including Prof. Tatsuo Itoh, Prof. Mona Jarrahi and Prof. Troy Carter, for their time and effort to review my PhD study. Especially, many times Prof. Itoh encountered me in the hallway, he was kind to ask about my progress and provide his suggestions not only in my technical difficulty but also in my career planning.

I also enjoy my friendship with the students around my lab, including Kirti Dhwaj, Brandon Choi, Michael Wu, Daisong Zhang, Ning Wang, Luyao Xu, Jacky Chan, Brad Liu, and Yinuo Xu. They spent a lot of happy time with me discussing technical issues or simply everything about life. I also specially thank my roommates who spent part of my five-year stay in Westwood, including Feng Liu, Pei Zhang, Shancheng Zhao, Jingzhou Zhao (What a coincidence we reunited at UCLA after high school!), Zhaoxing Bu, and Dong-in Kim.

More importantly, I thank my wife who recently married me after a 7-year, long-distance relation with me. Her love and faith in me are even beyond the greatness of this work. I would also like to thank my parents, especially my mom, who know me best and believe in me most. Their encouragement is my best gifts that help me through the difficult time.

Finally, I would like to acknowledge the research and financial support I have received from UCLA and off-campus sources including Northrop Grumman Corp. for research support, WIN Semiconductors Corp. for foundry service, IEEE MTT Society for Graduate Student Fellowship, and Skyworks Solutions, Inc. for intern opportunity.

VITA

2011	B.S. (Computer Engineering), Shanghai Jiao Tong University, Shanghai, China; B.S. (Electrical Engineering), University of Michigan, Ann Arbor, Michigan, USA.
2013	M.S. (Electrical Engineering), University of California, Los Angeles (UCLA), California, USA.
2012–2016	Research Assistant, Electrical Engineering Department, UCLA.
2014–2015	Teaching Assistant, Electrical Engineering Department, UCLA. Taught EE 101B (Electromagnetic Waves) for three quarters and EE 163A (Introductory Microwave Circuits) for one quarter.
2015	Student Intern, Skyworks Solutions Inc., Newbury Park, California, USA.

Publications

S. Qin and Y. E. Wang, "Parametric conversion with distributedly modulated capacitors (DMC) for low-noise and non-reciprocal RF front-ends," in *IEEE MTT-S Int. Microw. Symp. Dig.*, Seattle, WA, USA, Jun. 2013, pp. 1-3.

S. Qin, Q. Xu, and Y. E. Wang, "Nonreciprocal components with distributedly modulated capacitors," *IEEE Trans. Microw. Theory Techn.*, vol. 62, no. 10, pp. 2260-2272, Oct. 2014.

S. Qin and Y. E. Wang, "Broadband parametric circulator with balanced monolithic integrated distributedly modulated capacitors (DMC)," in *IEEE MTT-S Int. Microw. Symp.*

Dig., San Francisco, CA, USA, May 2016, pp. 1-4.

S. Qin and Y. E. Wang, "A nonreciprocal, frequency-tunable notch amplifier based on distributedly modulated capacitors (DMC)," in *IEEE MTT-S Int. Microw. Symp. Dig.*, San Francisco, CA, USA, May 2016, pp. 1-3.

S. Qin, M. M. Biedka, Q. Xu, and Y. E. Wang, "Broadband parametric circulators with monolithic integrated time-varying transmission lines (TVTL)," *IEEE Trans. Microw. Theory Techn.*, submitted.

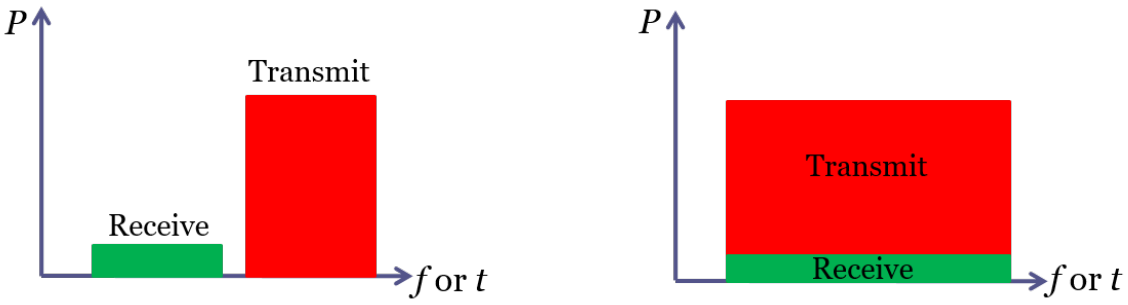
CHAPTER 1

Introduction

1.1 Challenges in Wireless Systems

Modern wireless communication systems have experienced tremendous success in measurable quantities such as better data rate, smaller physical size and lower monetary cost in the past few decades. While looking forward to the future fifth-generation (5G) communications, people are aggressive in achieving even better performances in wireless systems. However, challenges are there that many have to be resolved by non-conventional approaches to reach the seemingly high goals.

The well-known Shannon Theorem [1] states that the channel capacity, or the maximum data rate in a wireless channel, is proportional to the channel bandwidth and logarithmically increasing with the signal-to-noise ratio. Therefore, despite that the theorem is about the theoretical limit, one may argue that the most effective way to increase the data rate is to broaden the channel bandwidth. However, the frequency bandwidth is a precious resource and the spectrum usage cost composes the majority of the cost in, for example, our cellular-service bills. As the spectrum is highly restricted for civilian use, many technologies have been developed to create dimensions other than frequency to increase the data rate. The benefits from those technologies, however, are almost exhausted. As the limited spectrum resource is occupied by more and more crowded users, additional measures must be taken, especially if no more bands for civilian use are opened.



(a) (b)

Figure 1.1: Two types of wireless communications: (a) half-duplex; (b) full-duplex.

1.1.1 Half-Duplex v.s. Full-Duplex

One seeming flaw in the modern wireless systems is that RF signals are still transmitted and received either at different frequency bands or at different time frames in a wireless communication link between two consoles. This is regarded as the half-duplex communication. As illustrated in Fig. 1.1a, the transmitted signal may take no more than half of the accessible spectrum or time frame, while the received signal takes the other half, which is typical in cellular systems or in pulsed-radar systems, respectively. In either type of half duplex, the communication link utilizes only half (or practically, less than half) of the resource in frequency or in time. It is thus natural to question why we shouldn't take full advantage of the resource, which leads to the concept of full duplex.

Fig. 1.1b illustrates the full-duplex communication where signals are transmitted and received not only at the same time but also at the same frequency. The immediate benefit from realization of full duplex is the doubling in the channel capacity. (In fact, due to the practical frequency or time margin between the signal transmission and reception in half duplex, the theoretical capacity increase could be more than doubled.) However, full duplex has been long considered impossible especially in the long-distance wireless, because of the in-band self-interference caused by the large-power transmitted signal to the local receiver [2]. Many recent works, however, disagreed with the opinion, provided guidelines for sufficient

suppression of the self-interference, and demonstrated the advantage of full duplex over half duplex [3–8]. The suppression may involve interference cancellation in wireless propagation domain, analog circuit domain, and digital domain [8]. This work addresses the challenge in the wireless-propagation-domain suppression.

1.1.2 Bistatic (Separate-Antenna) v.s. Monostatic (Shared-Antenna)

A simple approach of providing suppression in wireless propagation domain is to separate the antenna for signal transmission and reception [3–5]. In addition, more antennas can be used for signal transmission [4] to realize narrowband, spatial cancellation at the received antenna. This is classified as bistatic (or separate-antenna) full duplex. The con of bistatic full duplex is obvious: antennas are still hard to be made small in physical size, and thus separate antennas are not favored in compact wireless systems. The involvement of multiple antennas for single-channel full duplex would also sacrifice the diversity that is necessary to overcome the fading caused by multi-path propagation. As a result, monostatic (or shared-antenna) full duplex [6, 7] is more appreciated.

Most shared-antenna systems require a device called duplexer to route the transmitted signal from the transmitter to the antenna and to route the received signal from the antenna to the receiver. The duplexer is also responsible for providing suppression from the transmitted signal to the receiver. Figure 1.2 shows a typical monostatic transceiver front-end with the duplexer in the center connecting the antenna, the transmitter and the receiver. In the half-duplex system, such duplexer could be a switch for time duplexing or a diplexer

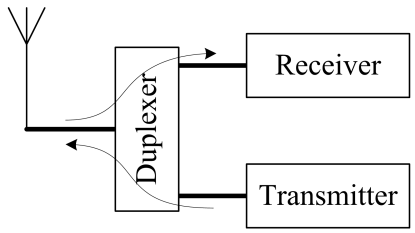


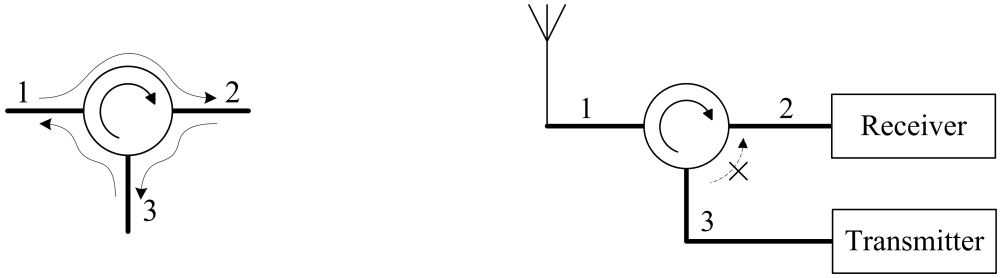
Figure 1.2: The duplexer in a shared-antenna transceiver front-end.

made of filters for frequency duplexing. For full duplex, a special type of duplexer called circulator is most commonly used. The performance of the circulator is crucial to a monostatic full-duplex system. The challenges in circulators are elaborated in the next section.

1.2 Circulators for Monostatic Full-Duplex

A circulator is known as a nonreciprocal component, as the signal flow in the forward direction is different from that in the reverse. A conceptual, three-port circulator shown in Figure 1.3a has ideally no mismatch in all ports, lossless insertion in the forward paths (namely, from port 1 to 2, port 2 to 3 and port 3 to 1) and no insertion in the reverse. The circulator in Figure 1.3a forms a clockwise circulation of the signal flow in three ports, but it is trivial to mention that counterclockwise circulators and those with more than three ports are also available.

When a circulator is connected as a duplexer shown in Figure 1.3b, some practical issues arise and there is much about what performances a good circulator should have. One of the concerns is about the inevitable leakage in the reverse path. In particular, the leaked signal from the transmitter (TX) to the receiver (RX), i.e., from port 3 to 2 in Figure 1.3b, need be as small as possible to prevent the receiver from being jammed by the transmitter. It is referred as the TX/RX isolation performance of a circulator, and high isolation, corresponding to small leakage from TX to RX, is highly desired. Another evaluation need be



(a) (b)

Figure 1.3: (a) A three-port circulator. (b) A circulator in a transceiver front-end.

made on the insertion loss and the noise performance of the receiving path, i.e., from port 1 to 2 in Figure 1.3b. Signals from the antenna to the receiver should gain little loss and/or additional noise through the circulator so that they could be detected properly. Other concerns may include the physical size of the circulator, or whether it can be integrated with the rest of the transceiver components, and the power capability for the transmitting path, as the transmitted signal's power can be very high. Last but not least, broadband circulator designs, if possible, are highly preferred.

1.2.1 Ferrite Circulators

Traditional circulators are built with nonreciprocal magnetic material such as ferrite and in the form of cylindrical cavities [9–12]. A ferrite circulator can have low receiving insertion loss and moderate TX/RX isolation. As it is a passive component, the receiving insertion loss of a ferrite circulator is equivalent to its noise figure. Ferrite circulators are also capable of handling high power. However, they are notorious with their bulky sizes and their narrow operation bandwidths, particularly when they are operated at the lower end of the microwave frequency spectrum. Above all, the process of ferrite is not compatible with any semiconductor integrated circuit (IC) technology, which makes the integration of the circulator with the rest of the RF front-end impossible.

1.2.2 Active Circulators

Early works of solid-state approaches to realize RF circulators rely on transistors that work in the conduction modes and whose transfer functions are nonreciprocal. They are classified as active or quasi-circulators [13–17]. Monolithic implementations of various active circulators have been proposed in [14–16]. In [17], a circulator was built with transistor-based metamaterial that has property resembling that of magnetic material. However, power saturation and noise-figure degradation are the common limitations of active, transistor-based circulator approaches [18–20], although the issue of power handling capability may be blurred with

the new, high-band-gap gallium nitride (GaN) semiconductor.

1.2.3 Recent Advances

Recently, there has been emergence of interests in achieving nonreciprocity in reciprocal structures or materials through time-modulation of transmission line or material property [21–33]. The original ideas were envisioned in the field of photonics [21–23], yet various configurations have been proposed to develop circulators in RF [24–32]. These works include angular momentum biasing [24–26], staggered commutation [27] and time-varying transmission lines (TVTL) [28–32]. The time-modulation is imposed through either reactance-based parametric modulation [24–26, 28–32] or high speed switching with passive switches [27]. The angular momentum approaches [24–26] mimic the nonreciprocal property of ferrite cavities with rotational parametric modulations. They exhibit high insertion loss and extremely narrow bandwidth similar to that of a cavity. The staggered commutation circulator [27] is constructed on a CMOS IC in the form of switched-capacitor N-path filters. The work is considered to be the first on-chip demonstration of a circulator, other than active circulators, without the use of magnetic material. However, the circulator requires additional load tuning at the ports for deep isolation and the achievable fractional bandwidth is also limited to a few percent due to the intrinsic bandwidth limitation of the N-path filter. In contrast, circulators based on TVTL [28–32] exhibit broadband isolation and low loss due to the non-resonant nature of the traveling wave structure, which is the main subject of this dissertation.

1.3 Circulators Based on TVTL and DMC

To gain an additional degree of freedom in designing nonreciprocal components like circulators, the time-varying property of transmission-line structures can be exploited. The directional dependency in the frequency mixing behavior of a nonlinear or time-varying transmission line (TVTL) can be utilized to separate signals overlapping in time, frequen-

cy, and space, but travelling in different directions. This is because when a unidirectional carrier or pump signal is injected in such a transmission line, the signal propagating in the same direction as the carrier will mix with the carrier in frequency, while the one against the carrier's direction will not. Consequently, the difference in the propagating directions of the signals is translated into the difference in modulation frequencies. Such difference allows the separation of the signals into different ports if a frequency diplexer is employed. A similar concept was proposed in the form of photonic links [23], where the transmit isolating receive photonic (TIPRx) links demonstrated bandwidth and isolation advantages over conventional circulators.

The frequency mixing behavior in TVTL is also related to the distributed parametric conversion effects that were intensively studied between the 1950s and 1960s [34–38]. The primary application then was to develop parametric amplifiers out of solid-state devices. The interest, however, diminished later when semiconductor transistors were invented and proven to be an overall better technology when gains and physical dimensions of amplifiers were emphasized. Recently, there has been a resurgence of interest [39–47] in utilizing parametric effects for both hybrid circuits and ICs by taking advantage of the intrinsically lower noise characteristics of the reactance-based components over the conductance-based components. Among those works, discrete parametric mixers [39–42] are investigated for applications such as frequency converters and multipliers. Distributed circuit architectures [43–45] are developed utilizing the degenerating parametric effects for resonators and narrowband amplifiers. In [46,47], Josephson junctions are employed as nonlinear inductors for nonlinear wave propagation or parametric amplification. In this work, the TVTL is treated as a distributed parametric amplifier, where the nondegenerating parametric conversion effects are utilized. Such effects are either enhanced or suppressed with the distributed circuit architecture to create nonreciprocity over a broad frequency band.

To develop practical TVTL, the distributedly modulated capacitors (DMC), which consists of a transmission line loaded with varactors diodes, is proposed. A microstrip-line DMC has been implemented and its results have been reported in [29, 31], where the broadband

isolation performance is consistent with the theoretical prediction has been demonstrated. However, the TVTL-based circulator has a lower cutoff frequency for isolation defined by the longest delay of the loaded transmission line. Miniaturization of the structure must be done in order to derive an on-chip implementation of such circulators at the lower RF spectrum. Moreover, the isolation performance of a uniformly modulated DMC follows a SINC function over a broad bandwidth with high sidelobes, indicating that high leakage level may appear over certain frequencies. The high-leakage problem may be overcome with either non-uniform modulations [31] that suppress the sidelobes of the SINC function or a balanced architecture [30, 32] that utilizes the phase diversity of the transmitter leakage in TVTL to further suppress it for a deeper isolation. In [32], a compact on-chip implementation of TVTL circulator is presented for the first time on a GaN IC through meandering the loaded microstrip lines. A balanced module with a pair of the DMC chips were also assembled and fabricated to achieve isolation greater than 30 dB over almost one octave of bandwidth. In this work, more details and updates regarding the work presented in [32] are provided by including a more complete description of the underlying theory and experimental results. In addition, a new MMIC design and implementation is presented here with superior measured performance than what was shown in [32].

1.4 Dissertation Outline

This dissertation is organized as follows. Chapter 2 provides the operating principles of the time-varying transmission line (TVTL) and its practical form as distributedly modulated capacitors (DMC). In Chapter 3, the DMC designs fabricated on a printed circuit board (PCB) and on a monolithic microwave integrated circuit (MMIC) are introduced with validation in simulation and measurement. After that, Chapter 4 introduces the concept of the balanced DMC that offers additional isolation for circulator application. A prototype has been tested by assembling a pair of DMC MMICs with commercially off-the-shelf (COTS) quadrature hybrids and diplexers. The measured performance of the balanced DMC validates the isola-

tion improvement offered by the balanced architecture. Finally, Chapter 5 summarizes the findings and concludes this work.

CHAPTER 2

Basics: TVTL and DMC

2.1 Transmission Line with Time-Varying Capacitance

The theory of an infinitely long transmission line whose reactance is time varying has been well studied in [35, 36, 48], under the scope of traveling-wave parametric amplifiers. The basic formulations are recaptured here to illustrate the underlying operating principle of the proposed nonreciprocal components based on the similar parametric effects.

Fig. 2.1 shows a lumped-element circuit model for a lossless transmission line with time-varying capacitance. The Telegrapher's equations, including the time variation of the capacitance per unit length in the time-varying transmission line (TVTL), can be written as

$$\frac{\partial v(z,t)}{\partial z} = -L' \frac{\partial i(z,t)}{\partial t}, \tag{2.1a}$$

$$\frac{\partial i(z,t)}{\partial z} = -\frac{\partial [C'(z,t)v(z,t)]}{\partial t}, \tag{2.1b}$$

where L' and C' are inductance and capacitance per unit length of the TVTL, respectively.

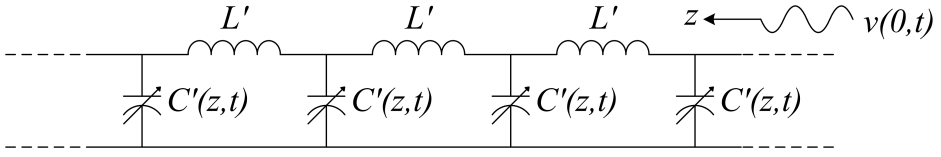


Figure 2.1: Time-varying transmission line where the capacitance per unit length is a function of time and space.

Rearranging the equations, one can obtain

$$\frac{\partial^2 v(z,t)}{\partial z^2} = L' \frac{\partial^2 [C'(z,t)v(z,t)]}{\partial t^2}. \tag{2.2}$$

When the capacitance is modulated by a single-tone carrier wave traveling in the $+z$ direction at the angular frequency ω_m (the subscript "m" means modulation), the capacitance per unit length, under the linear modulation assumption, can be written in a general form as

$$C'(z,t) = C'_0 + C'_m \cos(\omega_m t - \beta_m z + \phi_m), \tag{2.3}$$

where C'_0 is the mean capacitance per unit length, C'_m is the amplitude of the capacitance variation per unit length, and β_m is the phase constant of the carrier with a phase velocity of $v_m = \omega_m/\beta_m = 1/\sqrt{L'C'_0}$. The carrier wave does not carry information. It is assumed that the carrier behaves as a pump signal with uniform amplitude along the transmission line, which drives the time variation of the transmission line capacitance in a traveling-wave fashion.

Now assume a signal wave is launched into the same transmission line propagating toward the $+z$ direction at the angular frequency ω_s. The signal is mixed up and down with the capacitance modulation signal at ω_m, generating various harmonic and intermodulation terms. As the modulation frequency is normally chosen to be greater than the signal frequency ($\omega_m > \omega_s$), one can limit the discussions to three major tones: the input tone ω_s and both sidebands of the carrier $\omega_{m-s} = \omega_m - \omega_s$ and $\omega_{m+s} = \omega_m + \omega_s$. Furthermore, assume the variation of the capacitance is small and the transmission line is nondispersive over the bandwidth interested, i.e.,

$$\frac{\omega_s}{\beta_s} = \frac{\omega_{m-s}}{\beta_{m-s}} = \frac{\omega_{m+s}}{\beta_{m+s}} = \frac{\omega_m}{\beta_m} = v_p = \frac{1}{\sqrt{L'C'_0}}. \tag{2.4}$$

Given the boundary condition $v(0,t) = V_0 \cos(\omega_s t + \phi_s)$ at the input source, a solution of (2.2) can be

$$\begin{aligned} v(z,t) = V_s(z)\cos(\omega_s t - \beta_s z + \phi_s) + V_{m-s}(z)\sin(\omega_{m-s} t - \beta_{m-s} z + \phi_m - \phi_s) \\ + V_{m+s}(z)\sin(\omega_{m+s} t - \beta_{m+s} z + \phi_m + \phi_s), \end{aligned} \tag{2.5a}$$

where the amplitudes at the three tones are functions of the propagation distance expressed as follows:

$$V_s(z) = V_0 \cos\left(\frac{1}{2\sqrt{2}}\xi\beta_s z\right), \tag{2.5b}$$

$$V_{m-s}(z) = \frac{V_0}{\sqrt{2}}\frac{\beta_{m-s}}{\beta_s}\sin\left(\frac{1}{2\sqrt{2}}\xi\beta_s z\right), \tag{2.5c}$$

$$V_{m+s}(z) = \frac{V_0}{\sqrt{2}}\frac{\beta_{m+s}}{\beta_s}\sin\left(\frac{1}{2\sqrt{2}}\xi\beta_s z\right), \tag{2.5d}$$

where

$$\xi = C'_m/C'_0 \tag{2.5e}$$

is defined as the capacitance modulation index. More detail on the derivation of the solution is provided in Appendix A. The solution represents a gradual conversion process of the signal and the carrier energy into that of the frequency-converted signals. The magnitude of the input signal reduces gradually, while the magnitudes of the frequency-converted tones increase along the transmission line, until they reach to a distance of $z = \lambda_s/\xi\sqrt{2}$. The magnitudes of the up-converted output signals, expressed by (2.5c) and (2.5d), could reach the same or greater level than the input magnitude V_0, especially when a high carrier-to-signal frequency ratio $\omega_m/\omega_s(= \beta_m/\beta_s)$ is used, along with a sufficient modulation index ξ and the TVTL's electric length $\beta_s z$. This demonstrates that the TVTL works as an active, capacitive mixer for signals propagating in the same direction of the carrier, where the additional power for the active frequency-conversion gain must come from the carrier.

It is also worth noting that the solution in (2.5) represents the nondegenerating parametric case with the assumption that $\omega_m \neq 2\omega_s$. It does not involve exponential amplification along the transmission line like those described in [35, 36, 44, 45], where the high-gain characteristics of the degenerating parametric effect is exploited for development of parametric amplifiers or oscillators.

On the other hand, if the signal wave travels in the opposite direction to that of the carrier wave, no frequency-conversion terms can be obtained from (2.2), implying no energy is coupled between the input signal wave and the waves at the sidebands. The directional

dependency of the parametric conversion can be thus used to develop nonreciprocal components. Such directional dependency is capable of separating the signals traveling in opposite directions into different frequency bands at the two ends of the transmission lines. The resulting nonreciprocity is intrinsically broadband as it is not as resonance-based as a conventional ferrite circulator. It promises low-loss and low-noise characteristics as the TVTL only consists of reactance-based components.

Last but not least, the phase responses of the up-converted output signals trough the TVTL, as shown in (2.5a), contain the phase of the carrier with either the signal phase added to it at the upper sideband ($\phi_m + \phi_s$) or subtracted from it at the lower sideband ($\phi_m - \phi_s$). It means that by controlling the phase of the carrier ϕ_m, the TVTL can function as a phase shifter. It is shown in a practical TVTL model in Chapter 4 that such phase-shifting feature can be also utilized to create an additional dimension of phase diversity between the transmitted and received signals for the purpose of further isolation enhancement.

2.2 Distributedly Modulated Capacitors as a Circulator

The theoretical TVTL model can be approached in practice by periodically loading a conventional transmission line with variable capacitors in shunt, whose capacitances are modulated by a carrier wave that travels on the same or a different transmission line but at the same phase velocity as the signal wave, as illustrated in Fig. 2.2. The circuit is called Distributedly Modulated Capacitors (DMC) to manifest the modulation of those distributed capacitors by the traveling carrier wave. The DMC is a periodic structure, which is generally dispersive with its low-pass cutoff frequency determined by the loaded capacitance and the density of the capacitor placement [9]. The operating frequency can be selected to be much below its cutoff frequency so that the dispersion can be insignificant. The DMC bears all the features of a TVTL, including the property of up-converting the input signal to both sidebands of the carrier and the nonreciprocity in this up-conversion dictated by the traveling directions of the signal and the carrier waves. The dispersion of the DMC, on the other hand, can be

utilized to suppress the second harmonic of the carrier frequency, by designing the cutoff frequency below twice of the carrier frequency. This helps to prevent the formation of a shock wave in the carrier line, as reported in [37, 38].

In Fig. 2.2, a DMC is connected to an antenna on its right-hand side and a transceiver on its left-hand side. A carrier is injected from the right-hand side of the DMC. The antenna transmits and receives signals at the same frequency. The signal received by the antenna travels toward the transceiver, and this signal is up-converted by the carrier upon its arrival at the transceiver, because it travels in the same direction as the carrier. The transmitted signal, however, does not mix with the carrier. It remains at its original frequency all the way to the antenna. Therefore, the transmitted signal and the received signal are at different frequencies at the transceiver end of the DMC, and with a frequency diplexer, they can be separated into a transmitter and a receiver port. The device illustrated in Fig. 2.2 plays the role of a circulator, if the receiver operating frequency is modified accordingly. As aforementioned, the nonreciprocity of the device is obtained by taking advantage of the additional dimension of the time variance of the transmission-line property.

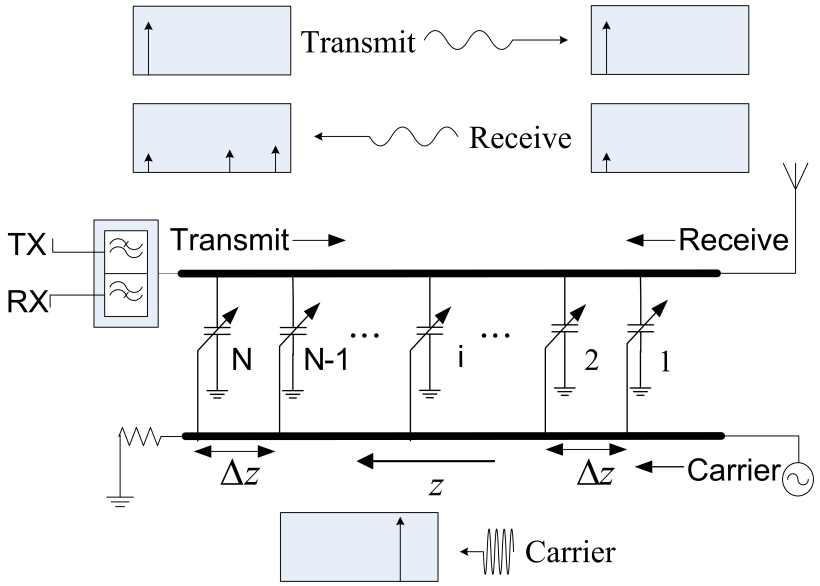


Figure 2.2: Concept of the proposed DMC for circulator application.

2.2.1 Isolation of Finite-Length DMC

For a finite-length DMC, the isolation between the transmitted signal and the received signal is limited. The theoretical performances of the conversion gain and isolation offered by the DMC can be derived. Each variable capacitor is considered as a capacitive mixer, which multiplies the carrier and the signal wave arriving at that capacitor [48–50]. In Fig. 2.2, N capacitors are distributed along the upper transmission line with equal separation length of Δz. Their capacitances are modulated by a single-tone carrier wave traveling in the $+z$ direction in the lower transmission line. For simplicity, only the first-order term of the capacitance modulation is considered, which implies the following relationship between the capacitance and the carrier voltage:

$$C(v_m) = C_d + C_1 \cdot v_m, \tag{2.6}$$

where C_d is the mean capacitance of the varactor, C_1 is the capacitance modulation sensitivity, which is defined as the amount of capacitance variation per unit voltage, and v_m is the voltage of the single-tone carrier wave, which follows a uniform amplitude distribution in the $+z$ direction, when the transmission line loss and the loss from the varactors are ignored. The voltage can be written in a complex form as follows:

$$v_m(z,t) = V_{m0}\cos(\omega_m t - \beta_m z + \phi_m) = \frac{1}{2}V_{m0}e^{j\phi_m}e^{j\omega_m(t-z/v_p)} + \frac{1}{2}V_{m0}e^{-j\phi_m}e^{-j\omega_m(t-z/v_p)}, \tag{2.7}$$

where ω_m is the angular frequency of the carrier, v_p is the phase velocity of the carrier wave on the transmission line, and β_m is the phase constant that satisfies $\beta_m = \omega_m/v_p$. The mean capacitance C_d can be assumed zero or, in practice, considered to be embedded into the periodic transmission-line structure. The capacitance modulated by the carrier voltage at the ith variable capacitor thus takes the form of

$$\begin{aligned} C(i\Delta z,t) &= C_1 \cdot v_m(i\Delta z,t) \\ &= \frac{1}{2}C_1V_{m0}e^{j\phi_m}e^{j\omega_m(t-i\Delta z/v_p)} + \frac{1}{2}C_1V_{m0}e^{-j\phi_m}e^{-j\omega_m(t-i\Delta z/v_p)}, \quad i = 1,2,...,N, \end{aligned} \tag{2.8}$$

where Δz is the length of the transmission-line section between each adjacent pair of variable capacitors. Let

$$C_i(t) = C_1 V_{m0} e^{j\phi_m} e^{j\omega_m(t - i\Delta z/v_p)} \tag{2.9}$$

be the complex-valued expression of the real-valued time-varying capacitance $C(i\Delta z, t)$ so that

$$C(i\Delta z, t) = \frac{1}{2} C_i(t) + \frac{1}{2} C_i^*(t), \tag{2.10}$$

where the superscript $*$ denotes the complex conjugate.

Assuming the same phase velocity for all the signal waves, as expressed in (2.4), one can express the voltages of the received (RX) and the transmitted (TX) signals in a similar way to the time-varying capacitance expression:

$$\begin{aligned} v^{\mathrm{RX}}(z,t) &= V_0 \cos\left(\omega_s t - \beta_s z + \phi_s^{\mathrm{RX}}\right) \\ &= \frac{1}{2} V_0 e^{j\phi_s^{\mathrm{RX}}} e^{j\omega_s(t - z/v_p)} + \frac{1}{2} V_0 e^{-j\phi_s^{\mathrm{RX}}} e^{-j\omega_s(t - z/v_p)} = \frac{1}{2} V^{\mathrm{RX}}(z,t) + \frac{1}{2} V^{\mathrm{RX}*}(z,t), \end{aligned} \tag{2.11}$$

$$\begin{aligned} v^{\mathrm{TX}}(z,t) &= V_0 \cos\left(\omega_s t + \beta_s z + \phi_s^{\mathrm{TX}}\right) \\ &= \frac{1}{2} V_0 e^{j\phi_s^{\mathrm{TX}}} e^{j\omega_s(t + z/v_p)} + \frac{1}{2} V_0 e^{-j\phi_s^{\mathrm{TX}}} e^{-j\omega_s(t + z/v_p)} = \frac{1}{2} V^{\mathrm{TX}}(z,t) + \frac{1}{2} V^{\mathrm{TX}*}(z,t), \end{aligned} \tag{2.12}$$

where

$$V^{\mathrm{RX}}(z,t) = V_0 e^{j\phi_s^{\mathrm{RX}}} e^{j\omega_s(t - z/v_p)}, \tag{2.13}$$

$$V^{\mathrm{TX}}(z,t) = V_0 e^{j\phi_s^{\mathrm{TX}}} e^{j\omega_s(t + z/v_p)}. \tag{2.14}$$

It is assumed in (2.11) and (2.12) that both received and transmitted signals are at the same frequency ω_s with identical amplitude V_0, but traveling in opposite directions.

When the received signal from the antenna is injected into the DMC, the voltage across each variable capacitor at the frequency of ω_s generates currents at both frequencies of $\omega_m \pm \omega_s$, because [50]

$$i_i^{\mathrm{RX}}(t) = \frac{d}{dt}\left[C(i\Delta z, t) v^{\mathrm{RX}}(i\Delta z, t)\right] = \frac{1}{2}\left[I_{i,m+s}^{\mathrm{RX}}(t) + I_{i,m+s}^{\mathrm{RX}*}(t) + I_{i,m-s}^{\mathrm{RX}}(t) + I_{i,m-s}^{\mathrm{RX}*}(t)\right], \tag{2.15}$$

where

$$I^{\mathrm{RX}}_{i,m+s}(t) = j\frac{1}{2}(\omega_m + \omega_s)C_i(t)V^{\mathrm{RX}}(i\Delta z, t), \tag{2.16a}$$

$$I^{\mathrm{RX}}_{i,m-s}(t) = j\frac{1}{2}(\omega_m - \omega_s)C_i(t)V^{\mathrm{RX}*}(i\Delta z, t) \tag{2.16b}$$

represent the complex-valued expressions of the currents generated at $\omega + \omega_s$ and $\omega - \omega_s$, respectively. The currents each split evenly and propagate towards the two ends of the transmission line, exciting voltages at both frequencies $\omega_m \pm \omega_s$ which are written as

$$\begin{aligned} V^{\mathrm{RX}}_{i,m\pm s}(t) &= -Z_B \cdot \frac{1}{2} I^{\mathrm{RX}}_{i,m\pm s}(t) \\ &= -Z_B \cdot j\frac{1}{4}(\omega_m \pm \omega_s)C_1 V_{m0} e^{j\phi_m} e^{j\omega_m(t-i\Delta z/v_p)} V_0 e^{\pm j\phi_s^{\mathrm{RX}}} e^{\pm j\omega_s(t-i\Delta z/v_p)} \\ &= -j\frac{1}{4}(\omega_m \pm \omega_s)Z_B C_1 V_{m0} V_0 e^{j(\phi_m \pm \phi_s^{\mathrm{RX}})} \cdot e^{j(\omega_m \pm \omega_s)(t-i\Delta z/v_p)} \\ &= -j \cdot g_{c,m\pm s} V_0 e^{j(\phi_m \pm \phi_s^{\mathrm{RX}})} \cdot e^{j(\omega_m \pm \omega_s)(t-i\Delta z/v_p)}, \end{aligned} \tag{2.17}$$

where Z_B is the Bloch impedance of the periodically loaded transmission line and

$$g_{c,m\pm s} = \frac{1}{4}(\omega_m \pm \omega_s)Z_B C_1 V_{m0} \tag{2.18}$$

are the conversion gains of each capacitive mixer for both sidebands of $\omega_m \pm \omega_s$. The up-converted signals from all the capacitive mixers arrive at both the transceiver and the antenna ends. They are, respectively, summed up after certain phase delays, which become

$$\begin{aligned} V^{\mathrm{RX}}_{\mathrm{transceiver},m\pm s}(t) &= \sum_{i=1}^{N} V^{\mathrm{RX}}_{i,m\pm s}\left[t - (N-i)\Delta z/v_p\right] \\ &= -j \cdot g_{c,m\pm s} V_0 e^{j(\phi_m \pm \phi_s^{\mathrm{RX}})} \sum_{i=1}^{N} e^{j(\omega_m \pm \omega_s)(t-N\Delta z/v_p)} \\ &= -jN g_{c,m\pm s} V_0 e^{j(\phi_m \pm \phi_s^{\mathrm{RX}})} \cdot e^{j(\omega_m \pm \omega_s)(t-N\Delta z/v_p)}, \end{aligned} \tag{2.19}$$

$$\begin{aligned} V^{\mathrm{RX}}_{\mathrm{antenna},m\pm s}(t) &= \sum_{i=1}^{N} V^{\mathrm{RX}}_{i,m\pm s}(t - i\Delta z/v_p) = -j \cdot g_{c,m\pm s} V_0 e^{j(\phi_m \pm \phi_s^{\mathrm{RX}})} \sum_{i=1}^{N} e^{j(\omega_m \pm \omega_s)(t-2i\Delta z/v_p)} \\ &= -j \cdot g_{c,m\pm s} V_0 e^{j(\phi_m \pm \phi_s^{\mathrm{RX}})} \cdot e^{j(\omega_m \pm \omega_s)t} \sum_{i=1}^{N} e^{-j2(\omega_m \pm \omega_s)i\Delta z/v_p}. \end{aligned} \tag{2.20}$$

It is obvious that the up-converted signals add in phase when they arrive at the transceiver end while they cancel with each other as they arrive out of phase at the antenna end. It is thus possible to retrieve the received information at the transceiver from the gross up-converted signal, which is expressed in the real-valued time domain as

$$v^{\mathrm{RX}}_{\mathrm{transciever},m\pm s}(t) = \frac{1}{2}V^{\mathrm{RX}}_{\mathrm{transciever},m\pm s}(t) + \frac{1}{2}V^{\mathrm{RX}*}_{\mathrm{transciever},m\pm s}(t)$$
$$= N g_{c,m\pm s} V_0 \sin\left[(\omega_m \pm \omega_s)(t - N\Delta z/v_p) + \phi_m \pm \phi_s\right]. \quad (2.21)$$

It is shown in Section 2.2.2 that (2.21) is consistent with up-converted terms in the TVTL solution in (2.5).

Similarly, when the transmitter injects a signal into the transmission line from the transceiver end in Fig. 2.2, the corresponding up-converted signal voltages generated at the ith capacitor in the complex-valued form are

$$V^{\mathrm{TX}}_{i,m\pm s}(t) = -j \cdot g_{c,m\pm s} V_0 e^{j(\phi_m \pm \phi^{\mathrm{TX}}_s)} \cdot e^{j[(\omega_m \pm \omega_s)t - (\omega_m \mp \omega_s)i\Delta z/v_p]}. \quad (2.22)$$

The up-converted TX signals arriving at the two ends of the transmission line are thus

$$V^{\mathrm{TX}}_{\mathrm{transceiver},m\pm s}(t) = \sum_{i=1}^{N} V^{\mathrm{TX}}_{i,m\pm s}\left[t - (N-i)\Delta z/v_p\right]$$
$$= -j \cdot g_{c,m\pm s} V_0 e^{j(\phi_m \pm \phi^{\mathrm{TX}}_s)} \sum_{i=1}^{N} e^{j[(\omega_\pm \omega_s)(t - N\Delta z/v_p) \pm 2\omega_s i\Delta z/v_p]}$$
$$= -j \cdot g_{c,m\pm s} V_0 e^{j(\phi_m \pm \phi^{\mathrm{TX}}_s)} \cdot e^{j(\omega_m \pm \omega_s)(t - N\Delta z/v_p)} \sum_{i=1}^{N} e^{\pm j2\omega_s i\Delta z/v_p}, \quad (2.23)$$

$$V^{\mathrm{TX}}_{\mathrm{antenna},m\pm s}(t) = \sum_{i=1}^{N} V^{\mathrm{TX}}_{i,m\pm s}(t - i\Delta z/v_p) = -j \cdot g_{c,m\pm s} V_0 e^{j(\phi_m \pm \phi^{\mathrm{TX}}_s)} \sum_{i=1}^{N} e^{j[(\omega_m \pm \omega_s)t - 2\omega_m i\Delta z/v_p]}$$
$$= -j \cdot g_{c,m\pm s} V_0 e^{j(\phi_m \pm \phi^{\mathrm{TX}}_s)} \cdot e^{j(\omega_m \pm \omega_s)t} \sum_{i=1}^{N} e^{-j2\omega_m i\Delta z/v_p}. \quad (2.24)$$

It is evident that the up-converted TX signals arrive out of phase at both ends of the transmission line and thus cancel each other when summed. This implies that the transmitted

signal should pass through the DMC with virtually no attenuation, as there is little conversion of the transmitted signal to other tones.

As the diplexer placed at the transceiver end in Fig. 2.2 separates the up-converted signal and the original signal injected by the transmitter, the isolation between the transmitter and the receiver can thus be defined with respect to either of the sidebands $\omega_m \pm \omega_s$:

$$\mathrm{ISO}_{m\pm s} = \left| \frac{V^{\mathrm{TX}}_{\mathrm{transceiver},m\pm s}}{V^{\mathrm{RX}}_{\mathrm{transceiver},m\pm s}} \right| = \frac{1}{N} \left| \sum_{i=1}^{N} e^{\pm j2\omega_s i\Delta z/v_p} \right| = \frac{1}{N} \left| \frac{1-e^{\pm j2\omega_s N\Delta z/v_p}}{1-e^{\pm j2\omega_s \Delta z/v_p}} \right| = \frac{\sin(\omega_s N\Delta z/v_p)}{N\sin(\omega_s \Delta z/v_p)}. \tag{2.25}$$

Such isolation is called transmitting-versus-receiving (TX/RX) isolation [23], as the up-converted TX leakage is normalized by the up-converted RX signal, which both are proportional to the capacitance modulation. The isolation also turns out equal in amount, whichever sideband is picked for signal reception. When the DMC is dispersive as in practice, however, the isolation may not follow strictly the SINC function in (2.25) and become different at different sidebands. A more general isolation equation without assumption of equal phase velocity or nondispersion is provided in Appendix B. When converted to decibel (dB), the isolation should be

$$\mathrm{ISO}_{m\pm s} \text{ in dB} = 20\log_{10}\left[\frac{\sin(\omega_s N\Delta z/v_p)}{N\sin(\omega_s \Delta z/v_p)}\right]. \tag{2.26}$$

The isolation is usually of negative value in dB as plotted in the figures shown in the later chapters, which is opposite to the conventional definition that describes the isolation in positive-dB value. However, in the text we comply with the convention so that the negative sign is often blurred as a common practice in many literatures, and the more negative in dB defined by this equation, the higher isolation is truly meant.

It should also be noted that (2.25) represents a Fourier transform relationship between the amplitude distribution of capacitance modulation and the frequency-dependent TX/RX isolation characteristics of the DMC. Such a relationship is similar to that between the antenna element excitations and the far-field radiation pattern of a linear phased array. A uniform capacitance modulation along the transmission line results in a discrete SINC

function in its frequency-dependent isolation characteristics as evidenced by (2.25), whose first null appears when the following condition is satisfied:

$$\omega_s N\Delta z/v_p = \pi \quad \Rightarrow \quad N\Delta z = \lambda/2. \tag{2.27}$$

Therefore, broadband isolation is achievable once the electric length of the DMC is longer than $\lambda/2$. However, high sidelobes may exist even in the isolation region and they decrease slowly as frequency increases, as it is designated by the SINC function in (2.25).

To obtain lower sidelobes, one may follow the strategy used in the field of phased-array pattern synthesis where a window is applied to the element excitations to reduce the radiation leakage after Fourier transform. It is equivalent to tapering the capacitance modulation amplitude in the DMC case. The complex-valued capacitance modulation at the ith variable capacitor, originally expressed as (2.9), is now multiplied with some weighting coefficient w_i:

$$C_i(t) = w_i C_1 V_{m0} e^{j\phi_m} e^{j\omega_m(t-i\Delta z/v_p)}, \quad i = 1, 2, ..., N. \tag{2.28}$$

The weighting coefficient w_i may be realized by using variable capacitors with different modulation slopes or by tapering the carrier wave voltage imposed on each capacitor. The isolation for the weighted DMC is thus

$$\left|\frac{V^{\mathrm{TX}}_{\mathrm{transceiver},m\pm s}}{V^{\mathrm{RX}}_{\mathrm{transceiver},m\pm s}}\right| = \left|\frac{\sum_{i=1}^{N} w_i e^{\pm j2\omega_s i\Delta z/v_p}}{\sum_{i=1}^{N} w_i}\right|. \tag{2.29}$$

A window generally results in lower sidelobes at the price of the increased main lobe. For example, one could follow a Dolph-Chebyshev window [51] in the selection of w_i in order to obtain a specified equal-sidelobe level in the isolation region, as later shown in Fig. 3.3.

2.2.2 Conversion Gain of Finite-Length DMC

As the up-converted signals are combined coherently at the transceiver end of the DMC, as illustrated in (2.21), the gains of the RX signal after up-conversion to both sidebands at $\omega_m \pm \omega_s$ are thus given by

$$\mathrm{G}_{m\pm s} = \left|\frac{V^{\mathrm{RX}}_{\mathrm{transceiver},m\pm s}(t)}{V^{\mathrm{RX}}(0,t)}\right| = N g_{c,m\pm s} = \frac{N}{4}(\omega_m \pm \omega_s) Z_B C_1 V_{m0}, \tag{2.30}$$

or in decibel,

$$\mathrm{G}_{m\pm s} \text{ in dB} = 20\log_{10}\left[\frac{N}{4}(\omega_m \pm \omega_s)Z_B C_1 V_{m0}\right]. \tag{2.31}$$

On the other hand, the conversion gains of the RX signal can be derived from the TVTL theory as in (2.5):

$$\left|\frac{V_{m\pm s}(z)}{V_0}\right| = \frac{1}{\sqrt{2}}\frac{\beta_{m\pm s}}{\beta_s}\sin\left(\frac{1}{2\sqrt{2}}\xi\beta_s z\right). \tag{2.32}$$

For short distance, i.e., $z < \lambda_s/\xi\sqrt{2}$, and small capacitance modulation index ξ, a small-variable approximation can be applied to the sinusoidal function in (2.32), which leads to

$$\left|\frac{V_{m\pm s}(z)}{V_0}\right| \approx \frac{1}{\sqrt{2}}\frac{\beta_{m\pm s}}{\beta_s}\cdot\frac{1}{2\sqrt{2}}\xi\beta_s z = \frac{1}{4}\xi\beta_{m\pm s}z. \tag{2.33}$$

The length of the transmission-line between two adjacent variable capacitors Δz in the DMC is assumed to be much shorter than the signal and the carrier wavelength to assure that both the signal and the carrier operate below the dispersive region. The following approximations are thus valid:

$$\xi = \frac{C'_m}{C'_0} \approx \frac{C_1 V_{m0}/\Delta z}{(C_d + C_{\text{line}})/\Delta z} = \frac{C_1 V_{m0}}{C_d + C_{\text{line}}}, \tag{2.34a}$$

$$\beta_{m\pm s} = \frac{\omega_m \pm \omega_s}{v_p} \approx (\omega_m \pm \omega_s)\sqrt{L'(C_d + C_{\text{line}})/\Delta z}, \tag{2.34b}$$

$$Z_B = \sqrt{\frac{L'}{C'_0}} \approx \sqrt{\frac{L'}{(C_d + C_{\text{line}})/\Delta z}}, \tag{2.34c}$$

where C_{line} is the capacitance of the transmission-line section between each neighboring pair of varactors. Substituting (2.34) into (2.33) yields

$$\left|\frac{V_{m\pm s}(N\Delta z)}{V_0}\right| \approx \frac{1}{4}C_1 V_{m0}(\omega_m \pm \omega_s)\sqrt{\frac{L'}{(C_d + C_{\text{line}})/\Delta z}}\cdot\frac{N\Delta z}{\Delta z} \approx \frac{N}{4}(\omega_m \pm \omega_s)Z_B C_1 V_{m0}, \tag{2.35}$$

which is in the identical form as (2.30). It is evident from both (2.30) and (2.35) that the up-conversion gain is proportional to the number of varactors as well as the amount of the capacitance variation, until the small-variable approximation can no longer hold. The aforementioned capacitive mixer analysis of the DMC can thus be considered as an approximation of the time-varying transmission-line theory for cases of short propagation distance, small capacitance modulation indices, and dense capacitor loading.

2.2.3 Noise Performance of Finite-Length DMC

Ideally, the DMC introduces no noise if both transmission lines and varactors are lossless. In reality, these two loss mechanisms do exist, by which thermal noise is introduced into the structure. To simplify the discussion, one can assume the DMC consists of ideal lossless transmission lines with lossy varactor diodes, in which case the loss of the transmission lines is incorporated into the varactor diode loss. The noise of the DMC arriving at the receiver port is a combination of two types of noise. The first type is the thermal noise emitted from the varactors' resistive loss at the original received frequency and then up-converted to the receiver band by the DMC. The second type of noise is the thermal noise directly emitted to the up-converted receiver band by the series resistance in the varactors. Both of them can be derived by assuming an equilibrium condition, i.e., that the amount of noise power generated by the structure equals the amount of noise the structure dissipates when a thermal resistor at the room temperature is assumed at the input. The equilibrium condition indicates that the amount of noise added by the structure at the original received signal frequency ω_s is

$$P_{n,s} = P_{n0}(1 - e^{-2\alpha_s z}), \tag{2.36}$$

where $P_{n0} = kT_0B$ is the noise power emitted by the thermal resistor at the room temperature T_0, and α_s is the attenuation constant of the transmission line loaded with the lossy varactors. The noise power can also be considered as a summation of the thermal noise power generated by the resistance of each varactor, which is

$$P_{n,s} = \frac{1}{Z_B}\sum_{i=1}^{N} v_{ni}^2 = \frac{N}{Z_B}v_n^2, \tag{2.37}$$

where v_{ni} is the noise voltage generated across the ith varactor and they are assumed to have the same root mean square (rms) value v_n. When the noise is up-converted to the receiver band after being mixed with the carrier signal, the noise of the first varactor is up-converted with the maximum gain as it will flow to the rest of $N-1$ mixers being up-converted. This,

substituted with (2.36) and (2.37), results in the total up-converted noise power to be

$$P_{n1,m\pm s} = \frac{g_{c,m\pm s}^2}{Z_B}\sum_{i=1}^{N}(N-i+1)^2 v_{ni}^2 = \frac{N(N+1)(2N+1)}{6Z_B} g_{c,m\pm s}^2 v_n^2$$
$$\approx \frac{N^3 g_{c,m\pm s}^2 v_n^2}{3Z_B} = \frac{N^2 g_{c,m\pm s}^2}{3} P_{n,s} = \frac{N^2 g_{c,m\pm s}^2}{3}(1-e^{-2\alpha_s z})P_{n0}. \quad (2.38)$$

The power of the second type of noise is obtained by the same equilibrium equation, however, at the up-converted frequencies:

$$P_{n2,m\pm s} = P_{n0}(1-e^{-2\alpha_{m\pm s} z}). \quad (2.39)$$

The noise figure is thus obtained as the ratio between the actual noise power versus the noise power from an ideal noiseless amplifier that has the same gain if a room temperature thermal resistor is placed at the input of either circuit, which is

$$\mathrm{NF}_{m\pm s} = \frac{P_{n,\mathrm{total}}}{N^2 g_{c,m\pm s}^2 P_{n0}} = \frac{N^2 g_{c,m\pm s}^2 P_{n0} + P_{n1,m\pm s} + P_{n2,m\pm s}}{N^2 g_{c,m\pm s}^2 P_{n0}}$$
$$= 1 + \frac{1}{3}(1-e^{-2\alpha_s z}) + \frac{1-e^{-2\alpha_{m\pm s} z}}{N^2 g_{c,m\pm s}^2}. \quad (2.40)$$

When loss is small, the following approximations can be applied:

$$1 - e^{-2\alpha_s z} \approx 2\alpha_s z = \frac{\beta_s z}{Q_s}, \quad (2.41a)$$

$$1 - e^{-2\alpha_{m\pm s} z} \approx 2\alpha_{m\pm s} z = \frac{\beta_{m\pm s} z}{Q_{m\pm s}}. \quad (2.41b)$$

In addition, the conversion gain from (2.33) indicates that

$$N^2 g_{c,m\pm s}^2 = \left(\frac{1}{4}\xi\beta_{m\pm s} z\right)^2. \quad (2.42)$$

The noise-figure formula can thus be rewritten (in decibel) as

$$\mathrm{NF}_{m\pm s} \text{ in dB} = 10\log_{10}\left(1 + \frac{1}{3}\frac{\beta_s z}{Q_s} + \frac{16}{\xi^2}\frac{1}{Q_{m\pm s}\beta_{m\pm s} z}\right), \quad (2.43)$$

where Q_s and $Q_{m\pm s}$ are quality factors of the loaded transmission line, respectively, at the original received frequency and the up-converted frequencies, which are estimated as

$$Q_s \approx \left(1 + \frac{C_{\mathrm{line}}}{C_d}\right) Q_{d,s}, \quad (2.44a)$$

$$Q_{m\pm s} \approx \left(1 + \frac{C_{\mathrm{line}}}{C_d}\right) Q_{d,m\pm s}, \quad (2.44b)$$

where $Q_{d,s}$ and $Q_{d,m\pm s}$ are, respectively, the quality factors of the varactor diodes at the original received frequency and the up-converted frequencies. From (2.43), one can see that the second type of noise dominates, until the structure is significantly longer than the wavelength so that the power of the first type of noise will rise to be comparable. It is also evident from (2.43) that varactors with high quality factors and high capacitance modulation indices will result in a low-noise DMC.

2.2.4 Power/Linearity Performance of Finite-Length DMC

It is evident from (2.30) that the receiving conversion gain of the DMC is proportional to the carrier voltage V_{m0}. In addition, (2.43) indicates that the capacitance tuning range of the varactors needs to be fully utilized to achieve a high capacitance modulation index ξ for the benefit of the noise figure. However, the selection of ξ is limited by the linear capacitance tuning range of the varactor device. If the tuning voltage required for a certain capacitance modulation index is between $\pm V_{m0}$, the required carrier power on the transmission line is thus

$$P_{\text{carrier}} = \frac{V_{m0}^2}{2Z_B}. \tag{2.45}$$

For typical GaAs varactors, a tuning voltage of approximately ± 3 V is often used for capacitance tuning with good linearity, which corresponds to a typical capacitance modulation index ranging from 15% to 25% and a carrier power requirement of 20 dBm on a 50-Ω transmission line. It should be noted that the carrier power serves only as a dynamic biasing voltage driving a capacitive load. It does not incur intrinsic power dissipation, except those dissipated on the transmission line and varactor resistance. The carrier power requirement can thus be relieved by either recycling the leftover carrier power at the end of the carrier line or using a buffer amplifier to drive each set of varactors to provide the needed carrier voltage. The carrier power dissipation on the transmission line can thus be minimized. The linearity of the DMC is generally more favorable to the transistor-based technology, as the receiving third-order intercept point (IP3) can be as high as the carrier power and the transmitting

IP3 can be much higher than the carrier power, as demonstrated by the simulation results in Section 3.1.1.

The carrier power requirement can be significantly lower without sacrificing the receiving conversion gain if more sensitive varactors such as CMOS varactors are used. The same capacitance modulation index can be achieved with a much smaller tuning voltage for these devices. However, the IP3 in those cases would scale down proportionally to the carrier power.

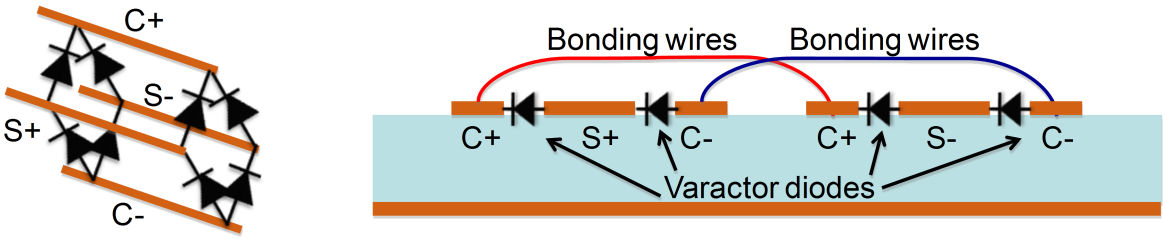
CHAPTER 3

Practical DMC Designs

3.1 DMC Design on PCB

One challenge in designing the DMC is that the three-port variable capacitors shown in Fig. 2.2 are either not available in practice or not sensitive enough to achieve high capacitance modulation index ξ. One simple realization of the DMC is to place both the carrier and the signal on the same capacitor-loaded transmission line, which would require diplexers with sharp cutoffs at the ends of the DMC to separate the signal and the carrier. This is what is implemented in our MMIC design introduced in Section 3.2, as complex design is highly constrained in the integrated circuit.

For the PCB design introduced in this section, we utilize two pairs of differential transmission lines loaded with reversely-biased varactor diodes in a double-balanced fashion. They are used to carry the carrier wave and the signal wave separately, as shown in Fig. 3.1a. C+



(a) (b)

Figure 3.1: DMC implemented in double-balanced fashion. (a) Transmission-line realization with two units shown. (b) Microstrip-line implementation with one unit shown.

and C- represent the carrier transmission lines, and S+ and S- represent the signal transmission lines. A simple analysis can show that these two transmission-line pairs are isolated from each other due to the symmetry, which leads to the fact that each transmission-line pair appears to be right on the virtual ground of the other one. The voltage of the carrier is considered as the dominant source modulating the capacitance of the varactor diodes loaded to the signal lines for two reasons. First, the carrier power is often selected to be much stronger than the signal power. Second, the double-balanced connection of the varactors achieves a certain degree of cancellation to the capacitance modulation caused by the signal voltage and its odd harmonic terms. The same concept can be realized on microstrip lines by splitting each carrier line and placing them symmetrically on both sides of each signal line, as demonstrated in Fig. 3.1b.

A 16-unit DMC with 64 variable capacitors evenly loaded between two pairs of transmission lines following the schematic of Fig. 3.1a is studied using Agilent ADS harmonic-balance simulations. The varactor model assumes a linear voltage-dependent capacitance. The transmission lines are ideal and each of them is four wavelengths long at the frequency of 6 GHz. The carrier frequency is selected to be 4.23 GHz. The characteristic impedance of the transmission line is 62.5 Ω and each capacitor has a DC capacitance of 0.36 pF with a maximum capacitance variation of $\pm$0.14 pF driven by 19-dBm carrier power per transmission line (22 dBm in total). The transmission line after the capacitor loading is calculated to have a Bloch impedance of 43 Ω [9]. The frequency-dependent Bloch impedance and phase delay per unit of the designed periodical structure are plotted in Fig. 3.2, which shows the cutoff frequency is slightly higher than 6 GHz, and the second harmonic of the carrier at 8.46 GHz is well rejected.

3.1.1 Simulated Performances

The TX/RX isolation, noise, conversion gain, and power/linearity performances of the proposed DMC are evaluated in simulation and compared with the theoretical prediction.

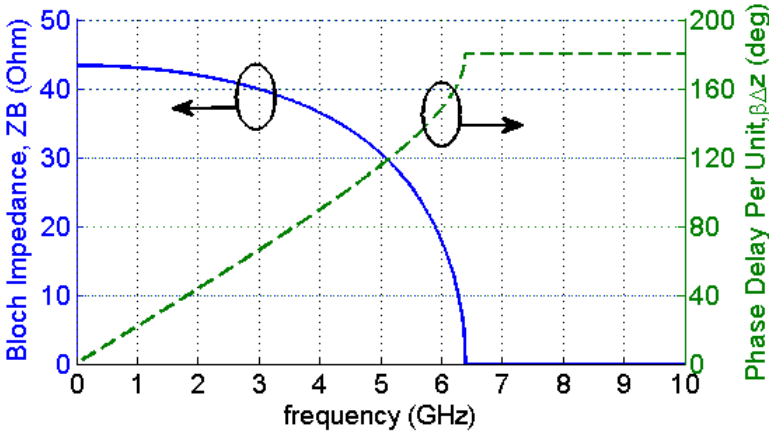


Figure 3.2: Dispersion behavior of the designed periodically loaded transmission line.

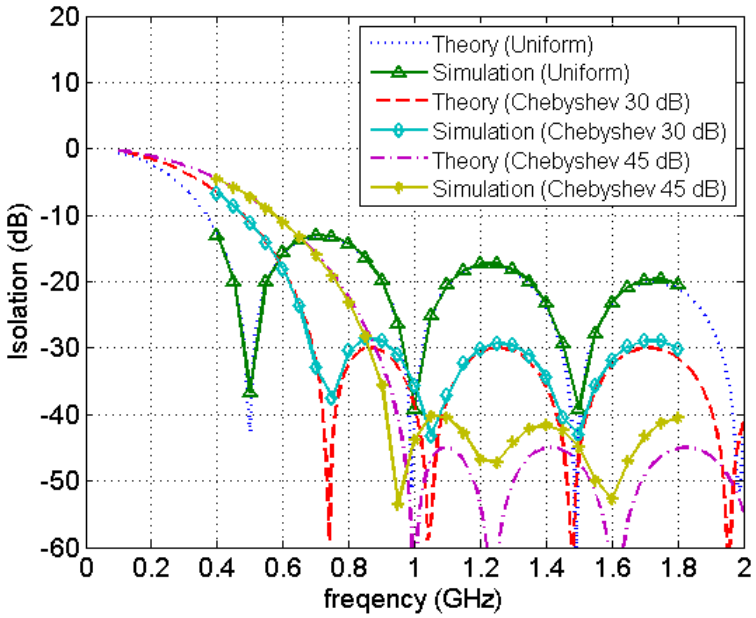


Figure 3.3: Comparison of TX/RX isolation at the sideband $\omega_m - \omega_s$, using uniform and nonuniform capacitance modulations in the DMC.

The TX/RX isolation of the proposed DMC design is simulated for both uniform and nonuniform capacitance modulation cases and the results are plotted in Fig. 3.3. The analytical results obtained from (2.25) and (2.29) are also plotted along with the simulation results. In the two nonuniform capacitance modulation cases, two Dolph-Chebyshev windows with 30-dB equal sidelobes and with 45-dB equal sidelobes are, respectively, applied. The analytical results agree well with those obtained from the circuit simulations except at particularly high isolation levels (> 45 dB) where the imperfect linearity of the capacitance modulation starts to affect the isolation performance. It is also observed in Fig. 3.3 that the uniform modulation leads to the lowest isolation cutoff frequency with the highest sidelobe at a level of -13 dB, while in nonuniform modulation cases, the sidelobes drop significantly at the price of the increased isolation cutoff frequency in the lower end.

The noise performance of the same DMC setup is simulated with a low-pass filter placed at the input to prevent the thermal noise at the higher frequency from entering the up-converted receiving band. The quality factor of the varactor diode is assumed to be 3000 at 0.5 pF and 50 MHz (the M/A-COM varactor model), and this quality factor is scaled down to higher frequencies for different capacitance value according to the inverse relationship $Q_d = 1/\omega R_d C_d$. The simulated noise figure as a function of the original received frequency along with its receiving conversion gain is plotted in Fig. 3.4 and compared with the theoretical prediction based on (2.43) and (2.30). Both the conversion gain and the noise figure simulation results agree well with theory, except that a small deviation is observed when the signal frequency is drawn very close to the cutoff frequency of the input filter (2 GHz). The conversion gain is positive in dB when the frequency is lower than 700 MHz and it drops to -4 dB at the higher end of the frequency band. The predicted noise figure is mostly in the range of 0.9 – 1 dB, which is considered to be excellent performance over such a broad bandwidth.

The power/linearity performance of the DMC under a large-drive signal is also simulated. Both the linear response and the cubic response as functions of the input power are plotted in Fig. 3.5. The signal's input frequency is 1 GHz for the linear-response test. For the two-

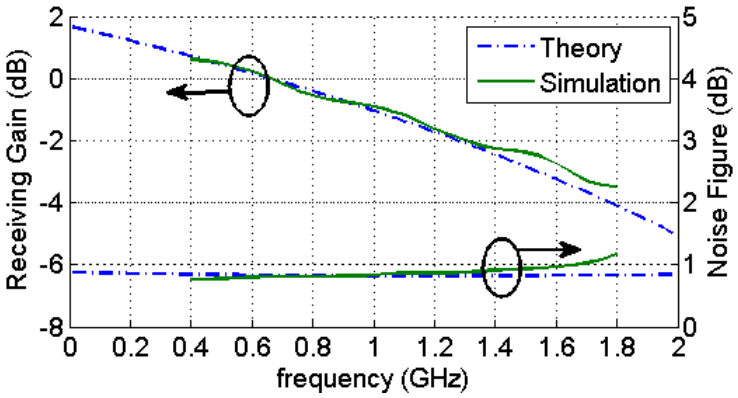


Figure 3.4: Simulated noise figure and conversion gain of the receiving signal at the sideband $\omega_m - \omega_s$ through the DMC.

tone cubic-response test, two equal-power signals with 30 MHz separation around 1 GHz are injected. It is observed that the received power starts to compress when the RX input approaches 10 dBm. The output IP3 of the receiving path is 20 dBm, comparable to the carrier power, while the simulated TX output IP3 is 33 dBm, much higher than the carrier power. Therefore, a safe margin for linear operation is to have the received signal power 10 dB lower than the carrier power, while the transmitted signal power is selected to be comparable to the carrier power.

3.1.2 Experimental Results

A DMC prototype is fabricated on a Rogers circuit board and shown in Fig. 3.6. The DMC is composed of 16 units of double-balanced varactor diodes. Each unit is realized according to the structure depicted in Fig. 3.1b, where four varactor diodes connected in a loop and fed by the transmission lines at the junctions. The dielectric constant of the substrate is 3.55. The total area occupied by the core DMC part is 128 mm $\times$ 10 mm. The design objective is to have the first null of the isolation curve at 500 MHz. From (2.27), the linear length of the structure is designated by half of the substrate wavelength at this first null. If the frequency is scaled up to 10 GHz and high-dielectric-constant substrate is used, the linear length of the structure will be 1/20th to 1/40th of the current one, which can fit in a chip

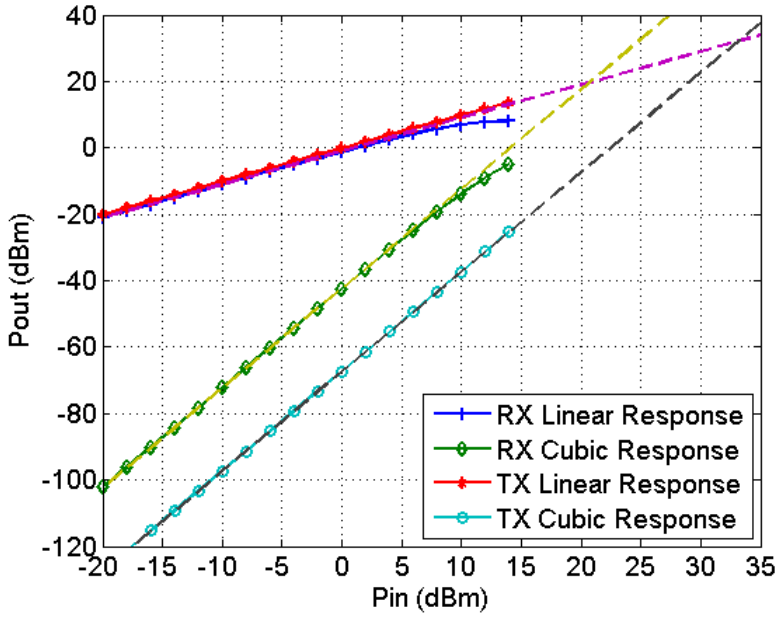


Figure 3.5: Simulated power/linearity performance of the receiving signal at the sideband $\omega_m - \omega_s$ and the transmitting signal at ω_s through the DMC.

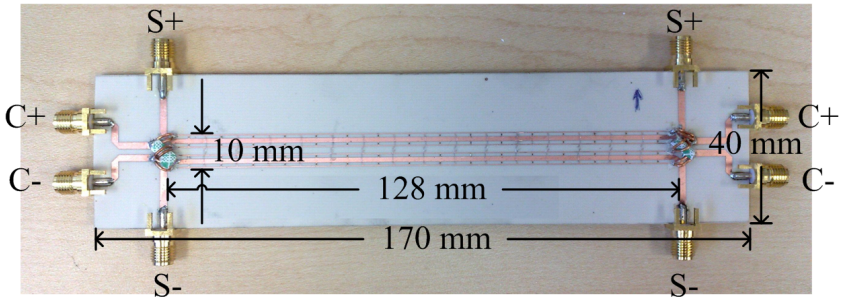


Figure 3.6: Photo of the DMC prototype on Rogers PCB with 16 units of double-balanced varactor diodes loaded on the microstrip lines.

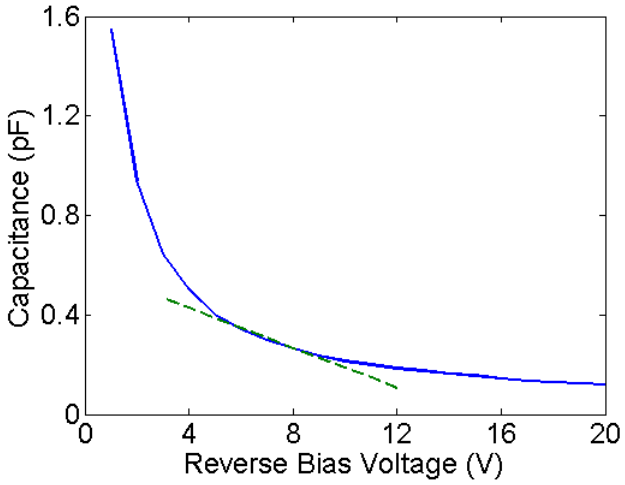


Figure 3.7: C-V curve of the MA46580 varactor [52].

area of 2 mm × 2 mm. The unloaded microstrip-line impedance is designed to be 125 Ω for each carrier line and 62.5 Ω for each signal line. The varactors are GaAs hyperabrupt junction diodes made by M/A-COM. Fig. 3.7 shows the capacitance-voltage relation of the varactor diodes. They are reversely biased with a voltage of 7.15 V to generate a mean capacitance of approximately 0.36 pF. Including the mean capacitance loading yields a 43-Ω Bloch impedance for each signal line and 80 Ω for each carrier line. The carrier voltage swing is ±3.45 V, which results in a capacitance variation of ±0.14 pF and an estimated capacitance modulation index of 0.18.

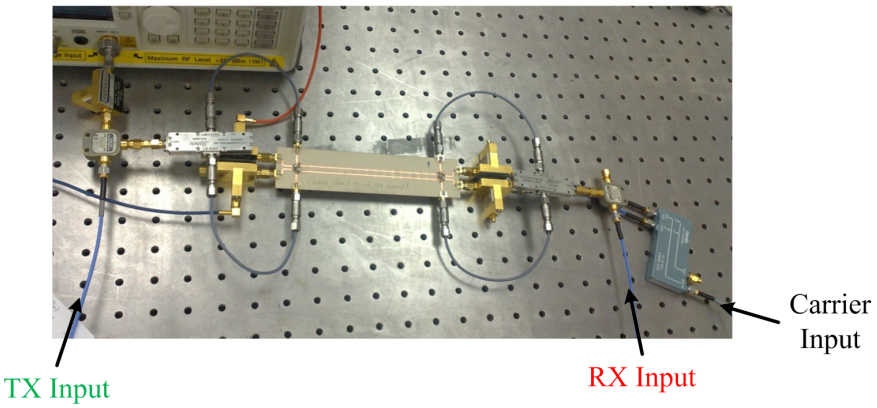
It should be noted that the phase-velocity match condition between the carrier and the signal wave, as indicated in (2.4), is crucial for good conversion gain and isolation performances. As the DMC is a periodic structure, one must be aware that the signal and the carrier do not operate in a dispersive region or anywhere close to the cutoff frequency of the structure. As the density of the capacitor loading determines the cutoff frequency of the periodical structure, a high operating frequency implies a dense placement of varactor diodes in the structure, which may enable IC-based implementations. Therefore, although the signal information can be retrieved from either or both of the sidebands at $\omega_m \pm \omega_s$, the received signal from only the lower sideband $\omega_m - \omega_s$ is considered in the following ex-

Label	Name	Model Number	Nominal Frequency Range
I	Synthesized Sweeper	HP 8340A	10 MHz – 26.5 GHz
O	Spectrum Analyzer	Agilent 8565EC	9 kHz – 26.5 GHz
D	DC Power Supply	Agilent E3620A	N/A
T	Bias Network	HP 11612A	45 MHz – 26.5 GHz
S	Power Splitter	HP 11667B	DC – 26.5 GHz
H	180° Hybrid Coupler	Narda 4346	2 GHz – 18 GHz
B	Broadband Balun	Marki BAL-0006	200 kHz – 6 GHz

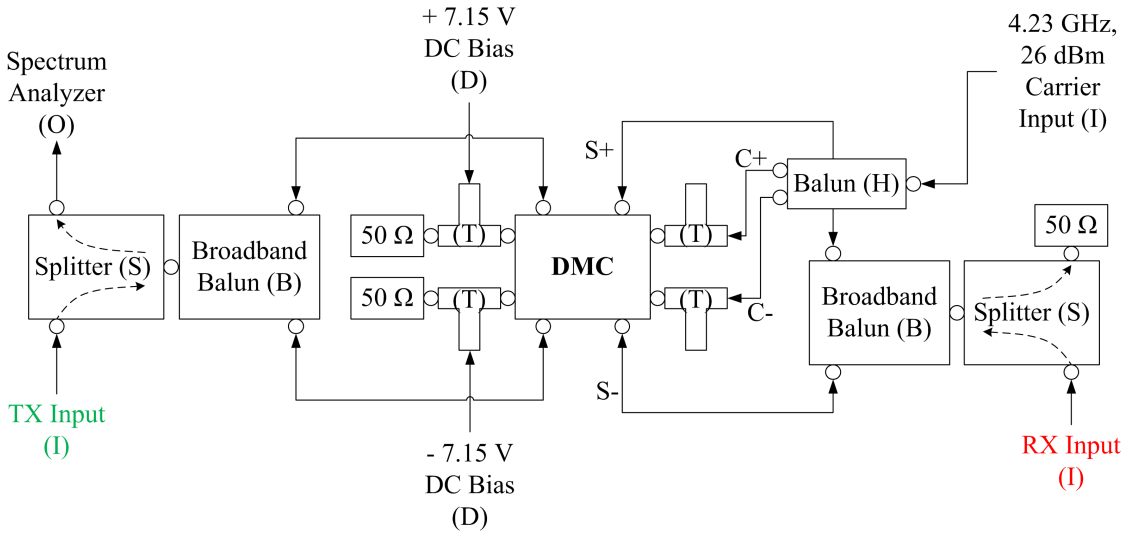
Table 3.1: List of the instruments and the components involved in the measurement for the DMC. Refer the labels to Fig. 3.8b.

periments. This is to accommodate a lower cutoff frequency of the periodic structure and sparser diode placements.

The measurement setup for the fabricated DMC is shown in Fig. 3.8. Baluns are used to convert the single-ended signals to differential input/outputs. Splitters are used to provide an extra path to the spectrum analyzers to monitor the signals. A carrier at the frequency of 4.23 GHz is injected into the carrier line from the left-hand side, with a power level of 26 dBm. As the balun has a loss of approximately 3 dB, plus the bonding wire and interconnect loss, the actual carrier power entering into the circuit is estimated to be lower than 23 dBm (20 dBm per line). A signal source at the level of -10 dBm is employed as the received signal injected into the line, if it is connected to the same side as the carrier, or the transmitted signal if it is connected to the other side. Spectrum analyzer 2 records the up-converted tones of the received signal and the transmitted signal as the outputs of the DMC to the transceiver. The instruments and the components used for the measurement are listed in Table 3.1. The performances of the DMC, such as the TX/RX isolation, the TX insertion gain, and the RX conversion gain, are evaluated based on the difference between these recorded signal levels and the original level of the input signal.



(a)



(b)

Figure 3.8: Measurement setup for the isolation and conversion gain performances of the DMC. (a) Photograph. (b) Diagram.

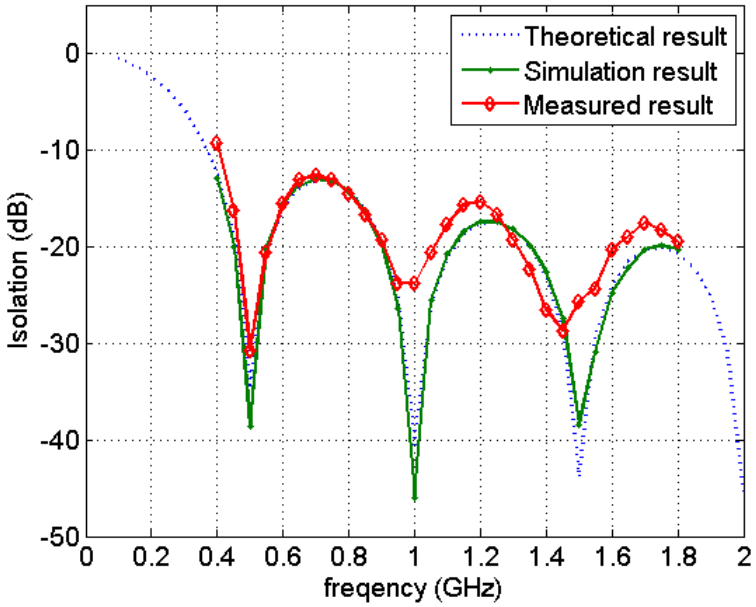


Figure 3.9: Measured TX/RX isolation in comparison with the simulation and analytical results for the sideband of $\omega_m - \omega_s$.

The measured TX/RX isolation with regard to the lower sideband $\omega_m - \omega_s$ is plotted in Fig. 3.9 in comparison with the results obtained from ADS circuit simulations theoretical derivation in (2.25). Due to the high carrier frequency and the narrow width of the transmission line, it is found that the transmission-line attenuation to the carrier wave cannot be ignored in analyzing the experimental results. A nonuniform weighting defined by the following equation is then applied when (2.29) is used to derive the analytical result:

$$w_i = e^{-\alpha_c i \Delta z}, \tag{3.1}$$

where α_c is the attenuation constant of the carrier line, which can be estimated through the measured insertion loss of the carrier, which is approximately 2 dB in this case. The isolation is measured to be greater than 13 dB over the frequency range of 0.45 – 1.8 GHz, which also agrees well with both the analytical result and the simulation result. The largest isolation of the DMC is achieved around the frequency of 500 MHz with an isolation of greater than 30 dB.

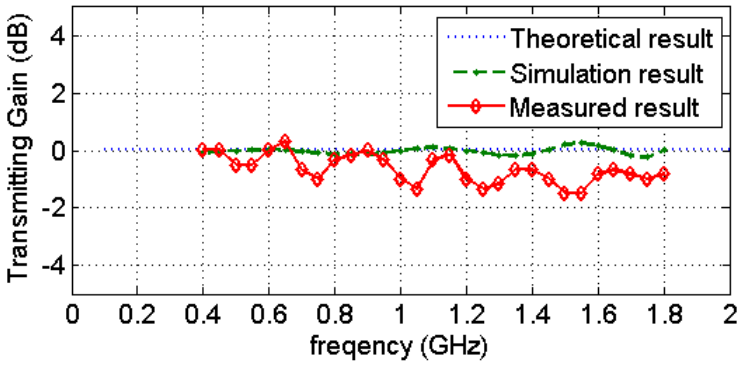


Figure 3.10: Measured TX insertion gain defined at the output to the antenna over the input from the transceiver at the original signal frequency.

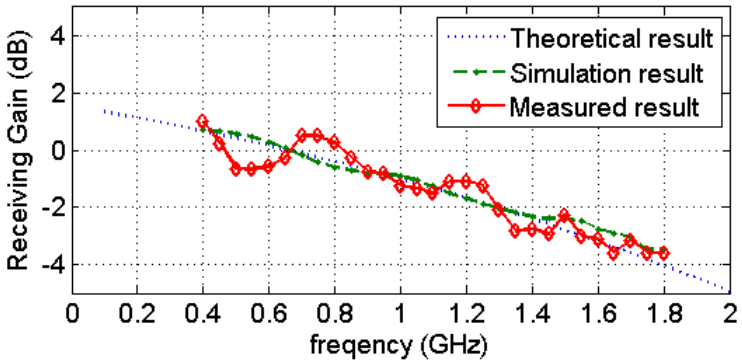
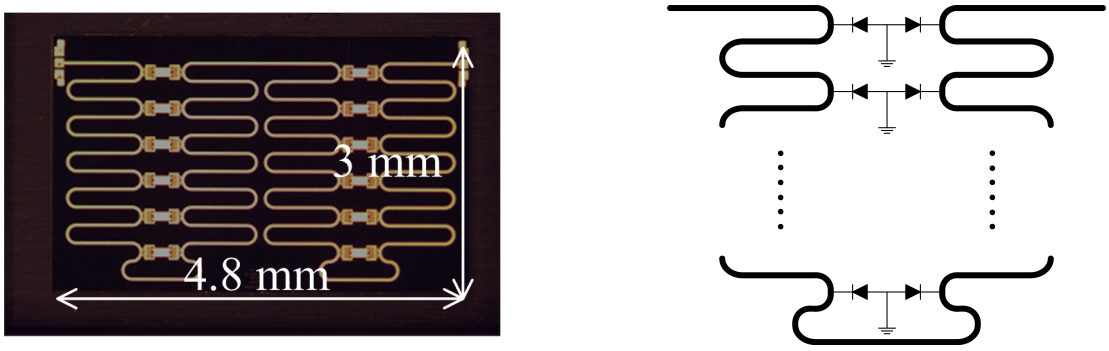


Figure 3.11: Measured RX conversion gain defined as the up-converted received signal output to the transceiver at $\omega_m - \omega_s$ over the original input from the antenna at ω_s.

Shown in Fig. 3.10, the measured insertion gain for the transmitted signal is in an average level of 0.5 dB and no more than 1.25 dB over the frequency range of 0.45 – 1.8 GHz, while the theoretical prediction and the simulation result are 0 dB. Fig. 3.11 shows the measured conversion gain for the receiving path, defined as the ratio between the voltage of the up-converted received signal at the lower sideband $\omega_m - \omega_s$ and the original received signal input at ω_s. The measured result agrees well with the simulation result and the analytical result. It is noted that the conversion loss increases along with the increase of the signal frequency as predicted by (2.30). This trend could be reversed in a design with higher transmission-line cutoff frequency, as the up-converted signal at the upper sideband can be used. The measured maximum RX loss is around 3 dB at the highest signal frequency of 1.8 GHz. The ripples observed in Fig. 3.10 and Fig. 3.11 are both believed to be caused by the imperfect match of transmission line impedance to 50-Ω ports and the imperfect calibration of the impedance mismatch introduced by the broadband baluns. It is also noted that a small amount of positive-dB gain is observed in the experiment for frequencies below 700 MHz, which is also predicted by the theory.

3.2 DMC Design on MMIC

The complexity of developing the DMC or the TVTL on a PCB is enormous as it requires attaching many diodes to transmission lines through wire bonds or other packaging techniques. On-chip integration of the DMC is beneficial in reducing the undesired parasitics and package uncertainty. Integration is also necessary in order for the proposed circulator to be deployed extensively in RF front ends of mobile communication systems such as those in full-duplex radios. In general, on-chip integration requires simple transmission line configurations for ease of miniaturization and reduction of parasitics and loss. It will be shown that simply meandering the transmission line can result in a fairly small IC area of a few squared millimeters for DMC circulators to operate throughout almost the complete cellular spectrum. Varactor diodes with large range of capacitance variation are desired which may



(a) (b)

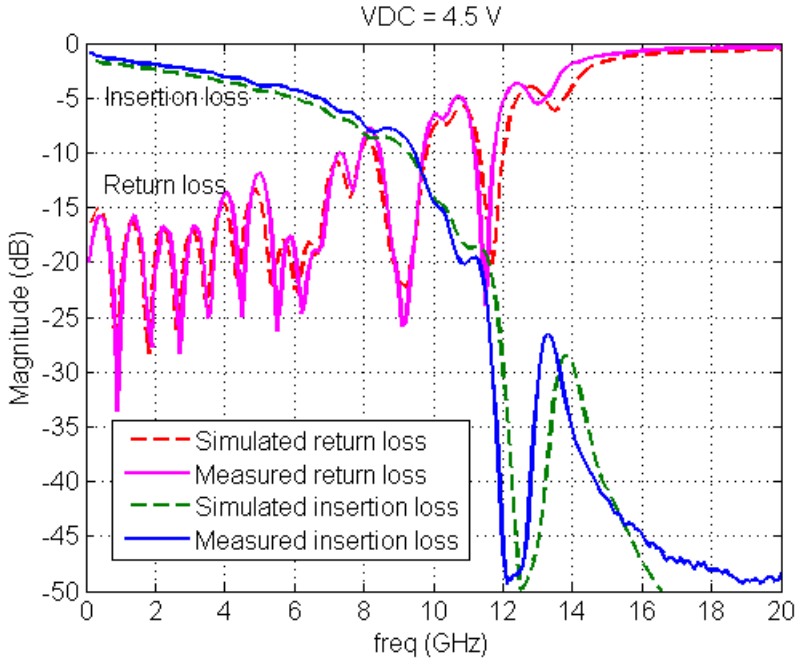
Figure 3.12: (a) Photo and (b) illustration of the DMC MMIC realized on 0.25 um GaN process. 24 GaN Schottky diodes are in shunt of the meandered microstrip line.

be derived from either a standard varactor process offered by some IC technologies or just a Schottky diode as part of the standard Field Effect Transistor (FET) process.

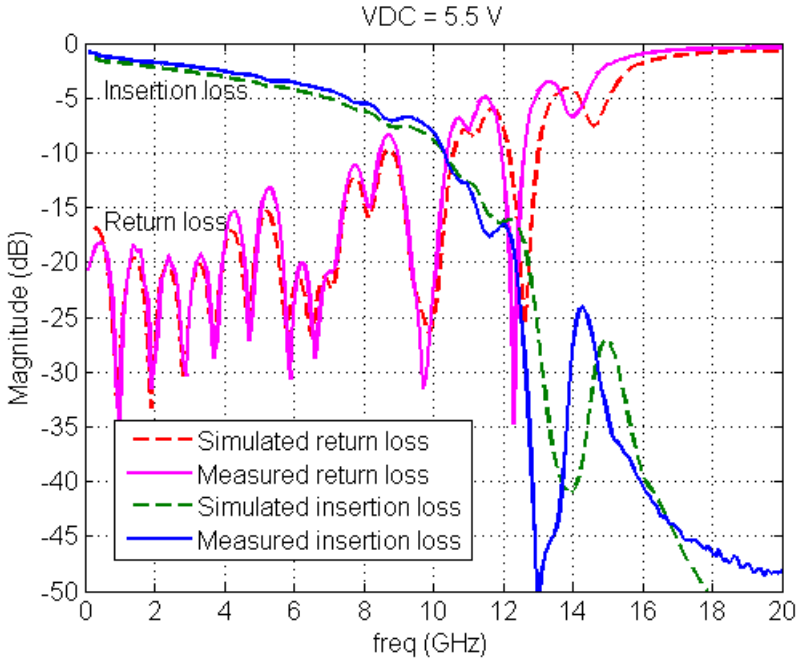
Shown in Fig. 3.12 is an example of the DMC MMIC fabricated with Northrop Grumman Aerospace System 0.25 um GaN HEMT technology. The intended operating frequency is from 0.5 GHz to 2.5 GHz. The physical size of the MMIC is 4.8 mm $\times$ 3 mm, which is about 1/100th of the area of the PCB version in Fig. 3.6. The MMIC is composed of 24 units of varactors periodically loaded on a meandered microstrip line, where both the carrier and the TX/RX signals propagate. The unloaded transmission line is 41 mm or two wavelengths long in total at 6 GHz on GaN/SiC substrate. 6 GHz is also the chosen frequency of the carrier that modulates the DMC. The characteristic impedance of the transmission line is 75 Ω. Each diode has a periphery of $8 \times 75 = 600$ um and it is estimated to have a capacitance of 0.4 pF biased at 4.5 V and 0.33 pF biased at 5.5 V. With the capacitors loaded in shunt, the Bloch impedance of the DMC as a periodic structure is approximately matched to 50 Ω.

3.2.1 Linear S-Parameter Test

The MMIC is mounted on a probe station for standard S-parameter test first to confirm its impedance match and passive loss, then followed by a mixer test to examine its parametric



(a)



(b)

Figure 3.13: Measured and simulated 2-port small-signal S parameters of the DMC MMIC without carrier pump but with varactor diodes biased at (a) 4.5 V; (b) 5.5 V.

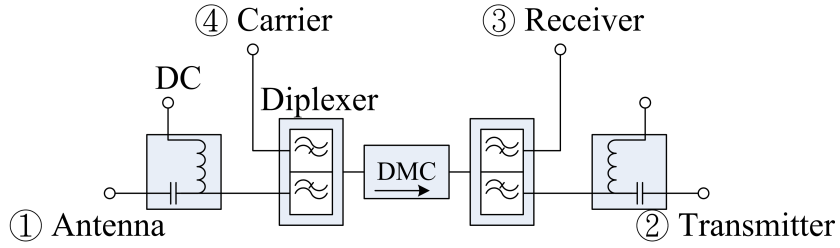


Figure 3.14: Measurement setup for the circulator performance test of the DMC MMIC.

frequency-conversion performances. Fig. 3.13 show the measured small-signal S parameters at two biasing voltages, 4.5 V and 5.5 V, including the return loss and insertion loss of the chip, compared with the simulation results incorporating the meandered microstrip line and through-substrate via structures simulated in ADS Momentum. The simulation results agree with the measured results very well, both indicating a fairly good impedance match at the frequency of 0.5 – 2.5 GHz. The 5.5-V-biased DMC is slightly better matched to 50 Ω than the one biased at 4.5 V. The measured passive insertion loss ranges from 1.3 dB to 2 dB over the same frequency range.

3.2.2 Nonlinear Frequency-Conversion Test – Circulator Performance

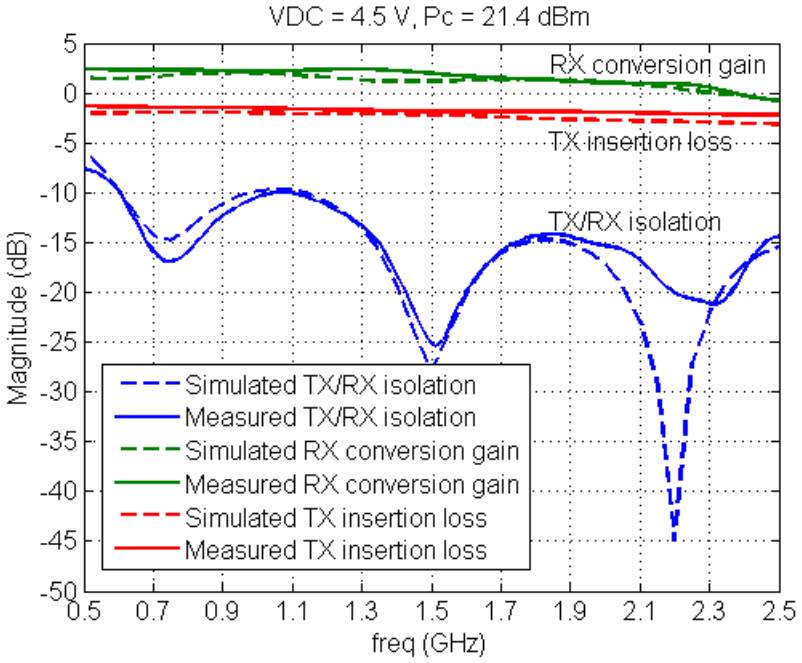
To measure the parametric circulator performance, an Agilent PNA-X with four ports and dual sources is used. A single-tone carrier at 6 GHz is generated by the PNA-X connected to Port 4 as denoted in Fig. 3.14. The carrier is combined through an external diplexer with another low-frequency RF signal generated from the second source of the PNA-X that is sweeping from 0.5 GHz to 2.5 GHz. The RF input is connected to Port 1 for RX test and Port 2 for TX test. The detailed test procedure is described as follows. For RX test, the combined signal is injected into the left-hand side of the MMIC as shown in Fig. 3.14. The external diplexer on the right-hand side of the MMIC separates the up-converted RX output from the low-frequency TX input and sends the output of Port 3 to the PNA-X for reading of the power at the up-converted frequency. This power versus the RF input power is defined as the RX conversion gain. For TX test, the low-frequency RF signal is injected

into Port 2, with the output of Port 1 at the original frequency versus the input read as the TX insertion loss, and the output of Port 3 at the up-converted frequency versus the input read as the TX leakage ratio. The TX/RX isolation is thus defined as the TX leakage ratio versus the RX conversion gain. As the input signal is swept from 0.5 GHz to 2.5 GHz, the up-converted band is thus at the carriers upper sideband from 6.5 GHz to 8.5 GHz. Note that the upper sideband is often preferred as a higher RX conversion gain can be potentially achieved as indicated by (2.5d).

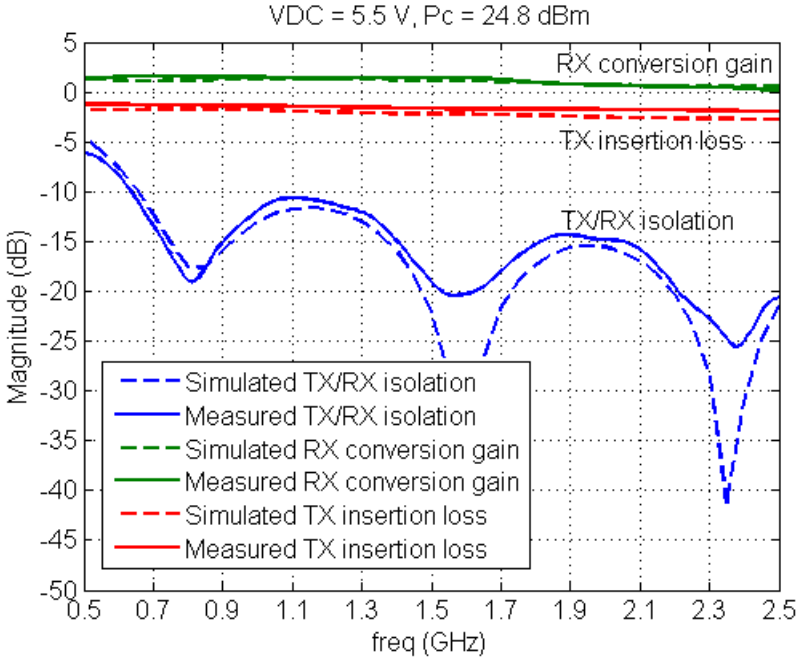
Fig. 3.15 display the measured parametric circulator performance of the DMC MMIC at the two conditions of varactors' DC bias at 4.5 V and 5.5 V and carrier power at 21.4 dBm and 24.8 dBm, respectively. In general, the RX signals, traveling along the carrier, achieve positive-dB conversion gain over the interested frequency in both biasing cases with the maximum gain of 2.4 dB. The DMC biased at 4.5 V achieves similar amount of parametric gain to that biased at 5.5 V but under 3-dB less carrier power drive. This is due to the increased capacitance variation sensitivity of the Schottky diodes at the lower DC bias, which could result in the same capacitance modulation index with less voltage swing. The measured RX conversion gain is compared favorably with the prior DMC MMIC design [32], due to the fact that the diode capacitance is being more sensitive to the driving voltage and a better yield process is used that assures the quality of the diodes.

The measured TX/RX isolations follow the theoretical SINC patterns as expected and are greater than 10 dB over the input frequencies of 0.7 – 2.5 GHz. The measured TX insertion loss of the MMIC is about 1.3 – 2 dB over the interested frequency, which is consistent with the passive insertion loss derived from the small-signal S-parameter measurements shown in Fig. 3.13. The insertion loss is mainly due to the high Ohmic loss of the thin microstrip line on the MMIC platform and the series resistance of the varactors, which may be improved with process of thicker metal and diodes with higher quality factors.

As the exact nonlinear capacitance model of the MMIC diode is not available, simulation results are generated with linear capacitance model with estimated capacitance modulation index $\xi = 0.47$ for 4.5-V biasing and $\xi = 0.43$ for 5.5 V, which fit well with the measured



(a)



(b)

Figure 3.15: Measured and simulated circulator performance of the DMC MMIC at (a) 4.5 V bias of the varactors and 21.4 dBm carrier power; (b) 5.5 V bias of the varactors and 24.8 dBm carrier power. The upper sideband $\omega_m + \omega_s$ is used for RX output.

conversion gain, insertion loss and isolation results in both cases.

CHAPTER 4

Isolation Improvement – Balanced DMC

When a finite-length DMC following the TVTL model is used as a T/R circulator, a remainder portion of the TX signal would be also up-converted to the receiving band and forms the TX leakage to the receiver. The leakage versus the up-converted RX signal, defined as the transmitting-versus-receiving (TX/RX) isolation in the DMC, follows a SINC function of the input signal frequency, as formulated in (2.25), when the uniform carrier modulation is assumed. In general, a broadband greater-than-13-dB isolation is expected from a single DMC due to its traveling-wave operation.

It has been shown in simulation (Fig. 3.3) that with certain non-uniform carrier modulation, greater than 40 dB isolation can be achieved. Regardless of the fabrication complexity, the non-uniform modulation approach, however, raises the lower cutoff frequency of the isolation and reduces the receiving conversion gain. A similar concept has been recently proposed with electro-optic modulators where broadband isolation is also achieved with both uniform and non-uniform modulations, yet the issues of insertion loss is unaddressed [23]. An alternative way to improve the isolation without suffering reduced bandwidth and receiving conversion gain is to utilize a balanced architecture [30, 32], which will be elaborated in this chapter.

4.1 Principles

The balanced DMC architecture can be utilized to add an additional level of isolation upon what can be achieved with a single DMC with theoretically little cost in its performance.

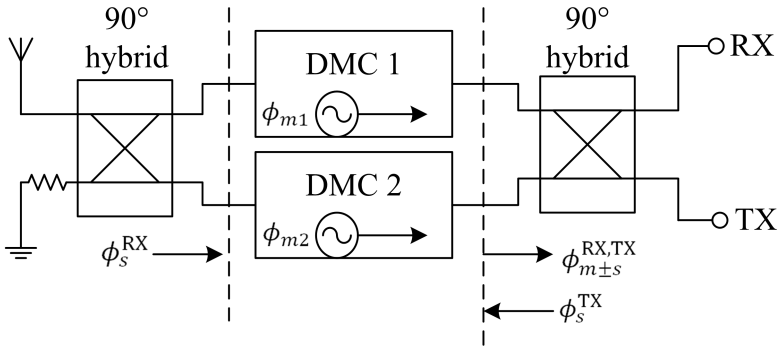


Figure 4.1: Block diagram of a balanced combo of two DMCs: the RX port is assigned at a different port of the 90° hybrid from TX.

Balanced structures have been used with circularly polarized antennas [6, 53] to isolate the transmitting and receiving functions in a full-duplex system by taking advantage of the phase diversity created at the different polarization components of the circularly polarized antenna. Here, without resorting to polarization diversity of the antenna, the balanced DMC architecture introduces phase diversity to the received signal through the carrier modulation. The balanced DMC consists of a pair of identical DMC units that are quadraturely fed with both the receiving and transmitting inputs, as shown in Fig. 4.1. The TX signal is split into two paths through the quadrature couplers on the transceiver side and is combined at the antenna port through the quadrature coupler on the antenna side. When carrier pumping is not turned on in the DMC units, the received signal from the antenna, though being split into two paths, must combine and travel to the TX port as governed by reciprocity. When the carrier is injected, the received information is now carried over to the up-converted frequency through the carrier modulation, and the up-converted RX signals through the two DMC units can combine constructively at the RX port, if the phase difference between the two carrier waves is properly set. Meanwhile, the TX leakage, being up-converted TX signals that return from the DMC units, would combine destructively at the RX port, which indicates an additional level of isolation.

In general, the carriers that modulate the DMC units can be chosen in phase or with 180° out of phase, depending on whether the lower or the upper sideband is used and of

which port the received signal is taken out. Following the circuit diagram shown in Fig. 4.1, the RX signal coming from the antenna is split by the first 90° coupler, becoming signals in the two paths with a relative phase difference of

$$\phi_{s,2}^{\mathrm{RX}} - \phi_{s,1}^{\mathrm{RX}} = 90^{\circ}. \tag{4.1}$$

Assume that the upper sideband is chosen to be the up-converted, output RX band. The split RX input signals entering the left-hand side of the DMC units experience the parametric conversion. According to the phase term in (2.5a) or in (2.21), the difference in the phase of the up-converted RX output signals at the right-hand side of the DMC units becomes

$$\phi_{m+s,2}^{\mathrm{RX}} - \phi_{m+s,1}^{\mathrm{RX}} = (\phi_{m2} + \phi_{s,2}^{\mathrm{RX}}) - (\phi_{m1} + \phi_{s,1}^{\mathrm{RX}}) = \phi_{m2} - \phi_{m1} + 90^{\circ}, \tag{4.2}$$

where ϕ_{m1} and ϕ_{m2} are the phases of the carriers that modulate the DMC units. Thus, it is evident that in order to combine the up-converted RX signals constructively at the RX port by the second 90° coupler, one must set $\phi_{m2} = \phi_{m1} - 180^{\circ}$, so that $\phi_{m+s,2}^{\mathrm{RX}} - \phi_{m+s,1}^{\mathrm{RX}} = -90^{\circ}$. Meanwhile, the TX signal coming from the TX port is split by the second 90° coupler, resulting in two TX signals with phase difference of

$$\phi_{s,2}^{\mathrm{TX}} - \phi_{s,1}^{\mathrm{TX}} = -90^{\circ}. \tag{4.3}$$

According to the phase term in (2.23), the finitely-small, up-converted TX signal in a finite-length DMC also has the same phase modulation effect as the RX signal. Therefore, with the same carrier phase condition as that in the RX case, the relative phase difference between the up-converted TX signals that are not completely suppressed by the DMC units and reflected back to the transceiver becomes

$$\phi_{m+s,2}^{\mathrm{TX}} - \phi_{m+s,1}^{\mathrm{TX}} = (\phi_{m2} + \phi_{s,2}^{\mathrm{TX}}) - (\phi_{m1} + \phi_{s,1}^{\mathrm{TX}}) = \phi_{m2} - \phi_{m1} - 90^{\circ} = 90^{\circ}. \tag{4.4}$$

Then after the second 90° coupler, these leakage signals combine destructively at the RX port, leading to an additional level of suppression of the TX leakage. Note that the transmitted signals at the fundamental frequency travel through the DMC units without being disturbed and combine constructively at the antenna port. Therefore, such balanced architecture can

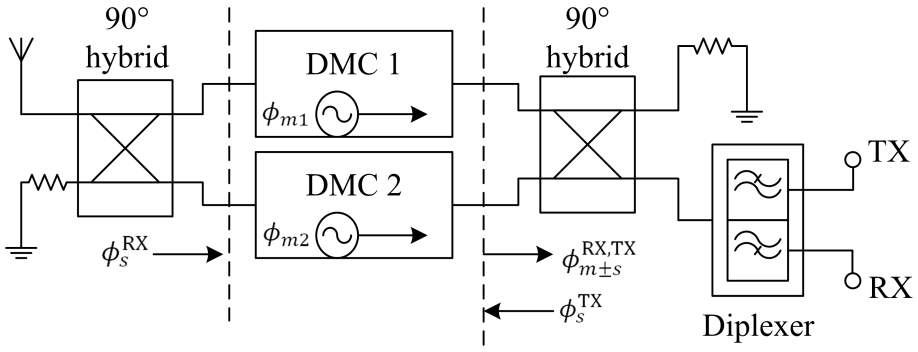


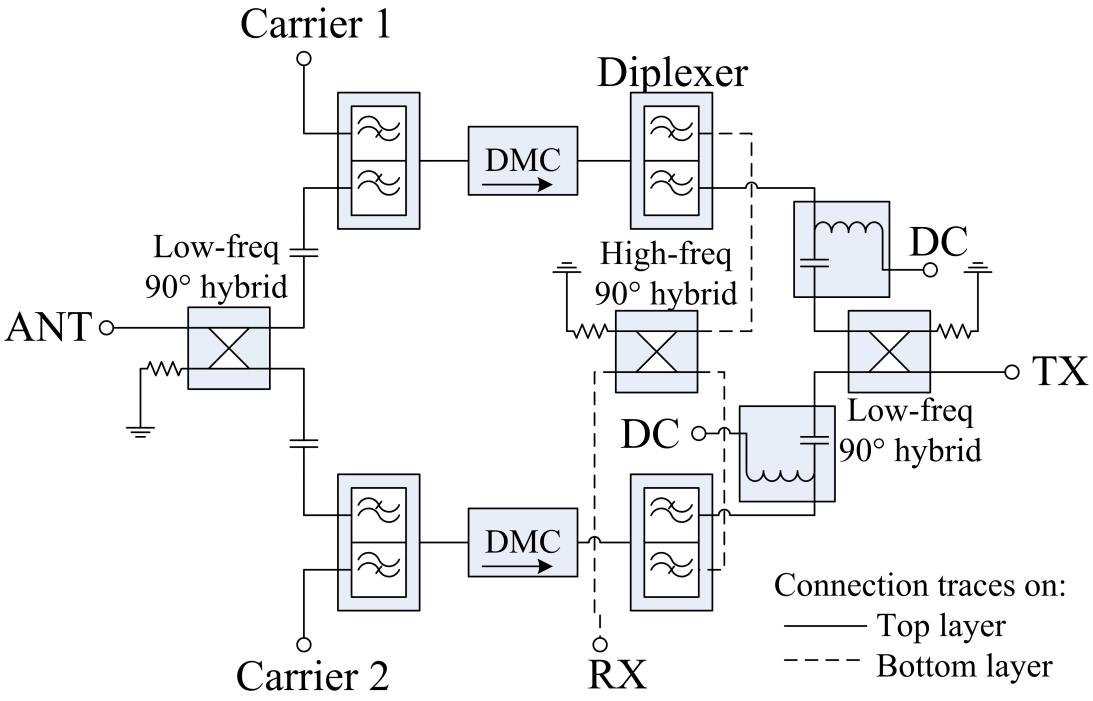
Figure 4.2: Block diagram of an alternative balanced DMC: the RX port is assigned at the same port of the 90° hybrid as TX until separated by the diplexer.

achieve additional isolation without compromising the bandwidth, RX conversion gain and TX insertion loss of the DMC except the increased complexity and loss from the external 90° couplers.

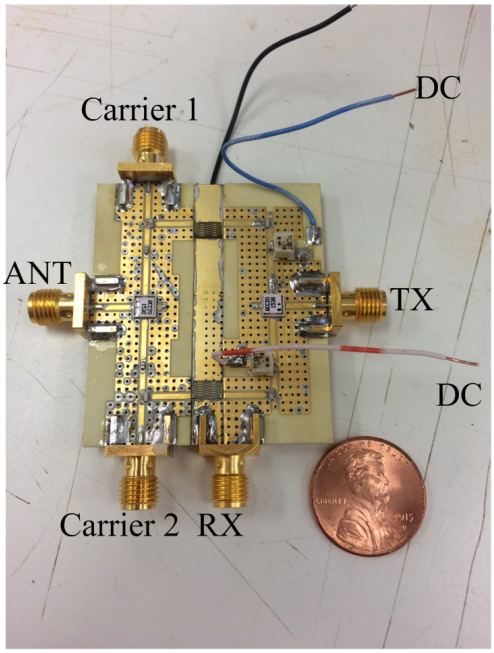
It has been shown that if the upper sideband is chosen for RX output, the carriers that modulate the two identical DMC units should be set 180° out of phase. It is left for the reader to prove that the carriers should be in phase if the lower sideband is chosen for RX output. In addition, the RX port may not be necessarily assigned at the other port of the second 90° hybrid than the TX port. It could be placed in the same port as that leading to TX and physically separated from TX by a frequency diplexer, as shown in Fig. 4.2, where then the combination of the carriers' phase condition and the RX output band should be interchanged. That is, the carriers should be in phase for RX output at the upper sideband or 180° out of phase for RX output at the lower sideband.

4.2 Implementation and Measured Results

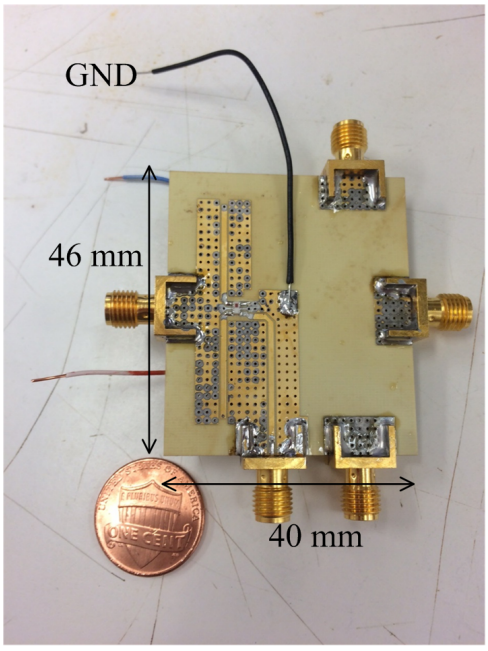
A balanced DMC module is developed by assembling a pair of the DMC MMICs introduced in Section 3.2 on a PCB with commercial off-the-shelf (COTS) hybrid couplers, bias tees and diplexers from Mini-Circuits listed in Table 4.1. The circuit diagram is illustrated in Fig. 4.3a, along with the photos of the fabricated balanced DMC module in Fig. 4.3b and 4.3c.



(a)



(b)



(c)

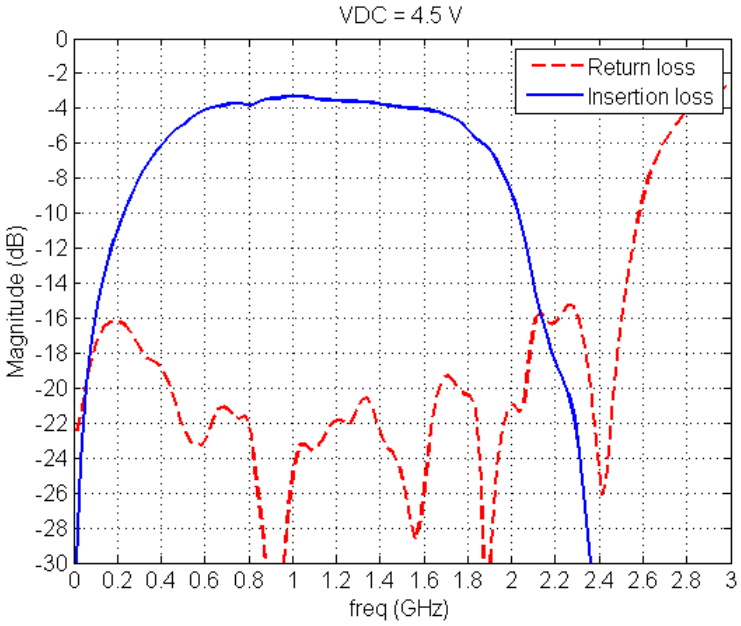
Figure 4.3: The balanced DMC prototype: (a) circuit diagram; (b) top view of the module; (c) bottom view of the module. The size of the fabricated prototype is compared with that of a U.S. penny.

Description	**Model Name**	**Nominal Frequency Range**
Low-freq 90° hybrid	Mini-Circuits QCC-20+	1.2 – 2.2 GHz
High-freq 90° hybrid	Mini-Circuits QCS-83+	4 – 8 GHz
Diplexer	Mini-Circuits LDPW-162-242+	DC – 1.65 GHz, 2.4 – 6 GHz
Bias Tee	Mini-Circuits TCBT-14+	10 MHz – 10 GHz

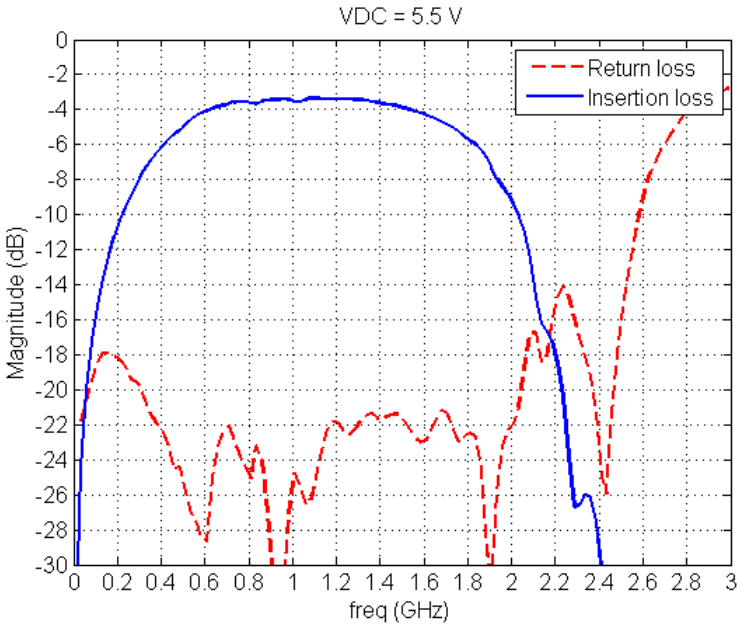
Table 4.1: List of COTS components used in the balanced DMC module in Fig. 4.3a.

Due to the challenge of finding a broadband quadrature hybrid coupler that can cover both input (low) and output (high) frequency bands, separate hybrid couplers are employed for each band, instead of just one proposed in theory. The circuit diagram basically follows the simplified diagram in Fig. 4.2, where if the two hybrid couplers connecting to the RX port and the TX port, respectively, were combined to be one, the RX port would be at the same port of the coupler as the TX port. As diplexers have been placed between the DMC and the hybrid couplers, the RX port is physically separated from the TX port. The quadrature hybrid for the output band is soldered at the bottom layer of the 3-layer PCB, while the rest of the components are mounted at the top layer. Through-hole vias are made to connect the traces at the top layer to those at the bottom layer. The board measures a dimension of 4.6 cm by 4 cm. Further miniaturization of the module is possible in the future with the state-of-the-art multi-chip module (MCM) packaging techniques such as Low Temperature Co-fired Ceramic (LTCC) process.

The 2-port small-signal S parameters measured between the TX and the antenna port of the module is shown in Fig. 4.4. It is evident that the operating frequency is limited by the bandwidth of the diplexer used in this module, which has a low-pass cutoff frequency of 1.65 GHz. Compared with the single DMC MMIC results in Fig. 3.13, the passband of the balanced DMC module is now limited to 0.6 – 1.8 GHz. The in-band insertion loss is also degraded by about 2 dB from that of the single MMIC due to the additional loss incurred by the off-chip components. Particularly, each diplexer and each hybrid coupler introduce about 0.5 dB, leading to a total loss of over 2 dB.

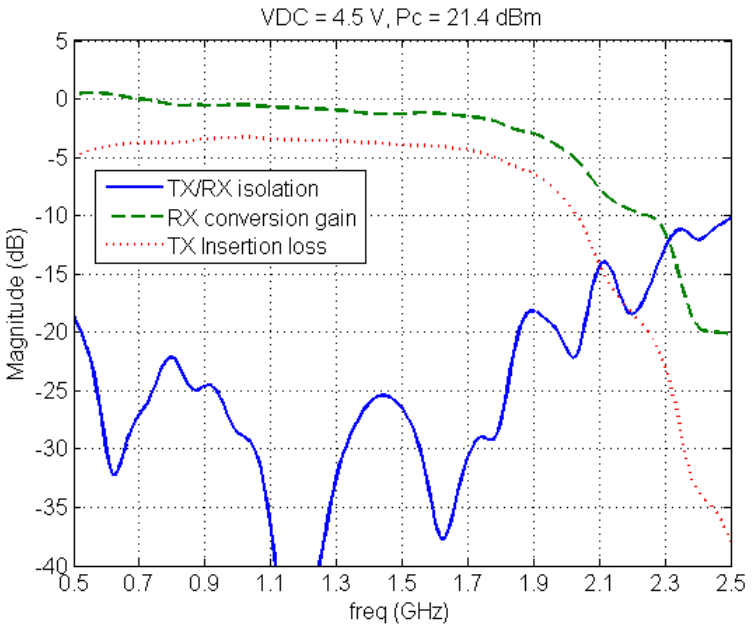


(a)

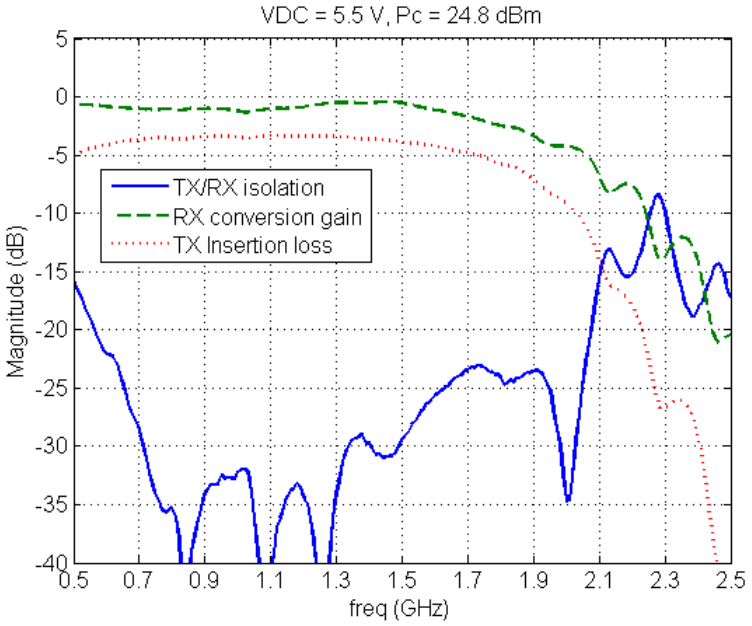


(b)

Figure 4.4: Measured 2-port small-signal S parameters of the balanced DMC module with varactors biased at (a) 4.5 V; (b) 5.5 V.



(a)

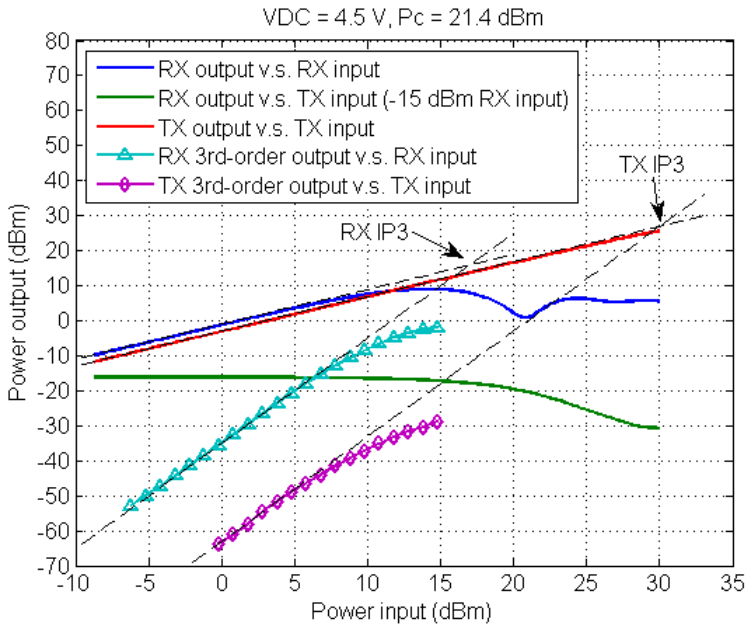


(b)

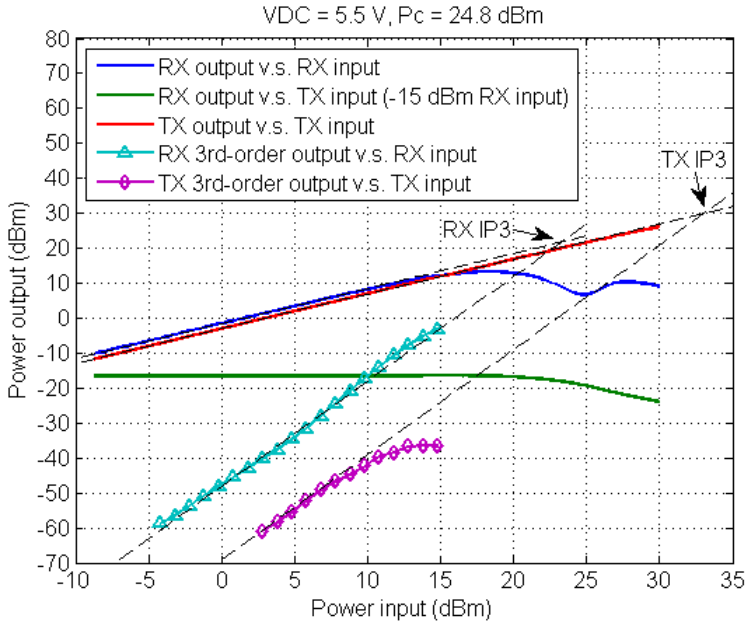
Figure 4.5: Measured circulator performance of the balanced DMC at (a) 4.5 V bias of the varactors and 21.4 dBm carrier power; (b) 5.5 V bias of the varactors and 24.8 dBm carrier power. The upper sideband $\omega_m + \omega_s$ is used for RX output.

The port-to-port measured results of the balanced DMC with parametric frequency conversion are shown in Fig. 4.5, based on the same DC and carrier conditions used for measurement of the single DMC chip in Section 3.2. The RX conversion gain becomes slightly less than 0 dB due to the loss of the off-chip components. Similarly, the TX insertion loss is increased to 4 – 5 dB throughout the interested frequency of 0.6 – 1.8 GHz. More than 20 dB TX/RX isolation is achieved throughout the whole band of 0.6 – 1.8 GHz, while more than 25 dB isolation is observed within the frequency range of 0.95 – 1.8 GHz when the DMC MMICs are biased at 4.5 V, and more than 30 dB isolation is observed over 0.8 – 1.3 GHz when the MMICs are biased at 5.5 V. Compared with the isolation results of a single DMC shown in Fig. 3.15, more than 15 dB improvement has been obtained. The low-frequency hybrid at the antenna-port side has a typical isolation of 25 dB between the two coupled ports which may limit the achievable TX/RX isolation of the balanced DMC module. Overall, the insertion loss and the isolation of the module can be further improved assuming that the off-chip components can be custom made and integrated on package.

The power/linearity performance of the balanced DMC module is also evaluated through large-signal measurements performed at the input signal frequency of 1 GHz. The measured results for both biasing cases are plotted in Fig. 4.6 and summarized in Table 4.2. It is evident that the DMC biased at a higher voltage can handle more power than that biased lower. At 5.5 V DC bias and 24.8 dBm carrier power, the output 1 dB compression point (OP1dB) is 26 dBm for TX of the balanced DMC module and 12 dBm for RX. One thing should be noted is that the RX conversion gain may also be compressed under a high TX input power as both TX and RX signals propagate in the same TVTL. In the measurement, it is observed that RX output power starts to compress by 1 dB when TX input power is beyond 22 dBm. The intermodulation products are also measured with the output third-order intercept point (OIP3) being 30 dBm for TX and 22 dBm for RX. It has been discovered in the experiments that the capacitance variation of the diode, though being sensitive during the biasing voltage range of 4 – 6 V, saturates quickly when the voltage drops below 3 V or greater than 7 V. This behavior may have caused the limited power handling of the DMC.



(a)



(b)

Figure 4.6: Measured circulator performance of the balanced DMC at (a) 4.5 V bias of the varactors and 21.4 dBm carrier power; (b) 5.5 V bias of the varactors and 24.8 dBm carrier power. The upper sideband $\omega_m + \omega_s$ is used for RX output.

	4.5 VDC, 21.4 dBm Pc	5.5 VDC, 24.8 dBm Pc
TX/RX isolation	$>$ 20 dB, 0.55 – 1.8 GHz $>$ 25 dB, 0.95 – 1.8 GHz	$>$ 20 dB, 0.6 – 2.07 GHz $>$ 25 dB, 0.66 – 1.6 GHz $>$ 30 dB, 0.72 – 1.3 GHz
RX conversion loss	$<$ 2 dB, 0.5 – 1.8 GHz Minimum -0.5 dB (gain)	$<$ 2 dB, 0.5 – 1.75 GHz Minimum 0.4 dB
TX insertion loss	$<$ 5 dB, 0.5 – 1.8 GHz Minimum 3.3 dB	$<$ 5 dB, 0.5 – 1.73 GHz Minimum 3.4 dB
TX OP1dB @ 1 GHz	25 dBm	26 dBm
RX OP1dB @ 1 GHz	7 dBm	12 dBm
TX input at RX P1dB @ 1 GHz	15 dBm	22 dBm
TX OIP3 @ 1 GHz	27 dBm	30 dBm
RX OIP3 @ 1 GHz	15 dBm	22 dBm

Table 4.2: Summary of the measured performance of the balanced DMC module.

With better optimized diode epitaxial structures, it is possible to optimize both the range and the sensitivity of the capacitance variation, which will lead to more robust performance of the DMC front-end in both efficiency and power handling in the future.

CHAPTER 5

Conclusion

This work presents the idea of utilizing nonreciprocity of the time-varying transmission line (TVTL) for broadband circulator application. The TVTL translates the direction difference of wave propagating in it into the difference in frequency based on its unidirectional frequency conversion property. A circuit with distributedly modulated capacitors (DMC) has been proposed to approach the TVTL and develop a broadband nonreciprocal microwave component functioning as a circulator. The DMC does not require ferrite and it would be readily integrated into a complete transceiver front-end even at the lower end of the microwave frequency spectrum.

Theoretical analyses based on both TVTL theory and the insight from distributed capacitive mixers are presented. They both lead to identical conclusions about the performances of the DMC, including the receiving conversion gain and the isolation. Simulations have validated the theory and demonstrated that the DMC features broadband synthesizable isolation, low conversion loss, low noise figure, and high IP3.

Microstrip prototypes of the DMC were fabricated both on Rogers PCB and on GaN MMIC to validate the performances and the compatibility of the DMC with IC technology. The PCB DMC has shown in measurement over 0.45 – 1.8 GHz more than 13 dB isolation, less than 3 dB receiving conversion loss at the lower sideband, and less than 1.25 dB transmitting insertion loss, while the MMIC DMC has demonstrates over 0.7 – 2.5 GHz more than 10 dB isolation, up to 2.4 dB receiving conversion gain at the upper sideband, and less than 2 dB transmitting insertion loss.

To further improve the isolation, a balanced combination of two DMC units is proposed

and implemented with the MMICs combined with COTS off-chip components. With the balanced architecture, the leakage through two DMC units is cancelled at the receiving port, resulting in an additional level of isolation enhancement. The balanced DMC module has exhibited deeper than 30 dB isolation for more than 50% of the bandwidth centered around 1 GHz and more than 25 dB isolation for almost a frequency ratio of 2:1 at 0.95 – 1.8 GHz. The power performance and linearity of the balanced DMC module is also measured and the results have demonstrated the promise of the DMC being a circulator in a full-duplex monostatic front-end that operates in the cellular frequencies.

APPENDIX A

Derivation of the TVTL Solution

Selected details on solving the time-varying transmission-line equations given by (2.2) and (2.3) are included here. The derivation follows similar steps to those in [35], except that time-varying capacitance is assumed instead of time-varying inductance in [35]. To solve the time-varying differential equations in (2.2), it is assumed that including signals at three frequencies, i.e., the original frequency and both sidebands, is sufficient. To make the derivation simple and concise, it is more convenient to represent the time-varying terms in a complex-number form similar to the phasor expressions used in solving linear time-harmonic electromagnetic systems. The time-dependent capacitance along the transmission line can thus be rewritten as

$$C'(z,t) = C'_0 + C'_m(z,t), \tag{A.1}$$

where

$$\begin{aligned} C'_m(z,t) = C'_m \cos(\omega_m t - \beta_m z + \phi_m) &= \frac{1}{2} C'_m e^{j\phi_m} e^{-j\beta_m z} e^{j\omega_m t} + \frac{1}{2} C'_m e^{-j\phi_m} e^{j\beta_m z} e^{-j\omega_m t} \\ &= \frac{1}{2} C'_m(z) e^{j\omega_m t} + \frac{1}{2} C'^{*}_m(z) e^{-j\omega_m t}, \end{aligned} \tag{A.2}$$

where

$$C'_m(z) = C'_m e^{j\phi_m} e^{-j\beta_m z} \tag{A.3}$$

complies with the phasor form of $C'_m(z,t)$ at ω_m, and the superscript $*$ denotes the complex conjugate. Furthermore, denote

$$\xi = C'_m / C'_0, \tag{A.4}$$

as the capacitance modulation index. Inserting (A.1) into (2.2) yields

$$\frac{\partial^2 v(z,t)}{\partial z^2} = L' C'_0 \frac{\partial^2 v(z,t)}{\partial t^2} + L' \frac{\partial^2 [C'_m(z,t) v(z,t)]}{\partial t^2}. \tag{A.5}$$

Given a sinusoidal input signal at the frequency ω_s, the signals generated at the sidebands of the modulation carrier, $\omega_{m-s} = \omega_m - \omega_s$ and $\omega_{m+s} = \omega_m + \omega_s$, are of the most significance. One may use

$$v_s(z,t) = \frac{1}{2}V_s(z)e^{j\omega_s t} + \frac{1}{2}V_s^*(z)e^{-j\omega_s t}, \tag{A.6a}$$

$$v_{m-s}(z,t) = \frac{1}{2}V_{m-s}(z)e^{j\omega_{m-s} t} + \frac{1}{2}V_{m-s}^*(z)e^{-j\omega_{m-s} t}, \tag{A.6b}$$

$$v_{m+s}(z,t) = \frac{1}{2}V_{m+s}(z)e^{j\omega_{m+s} t} + \frac{1}{2}V_{m+s}^*(z)e^{-j\omega_{m+s} t} \tag{A.6c}$$

to represent the signals at the three tones under consideration, where V_s, V_{m-s} and V_{m+s} comply with the phasor form of the time-domain signal expressions at ω_s, ω_{m-s} and ω_{m+s}, respectively. Inserting (A.2) and (A.6) into (A.5) leads to

$$\frac{d^2V_s(z)}{dz^2} = -\omega_s^2 L'C_0'V_s(z) - \frac{1}{2}\omega_s^2 L'C_m'(z)V_{m-s}^*(z) - \frac{1}{2}\omega_s^2 L'C_m'^*(z)V_{m+s}(z), \tag{A.7a}$$

$$\frac{d^2V_{m-s}^*(z)}{dz^2} = -\omega_{m-s}^2 L'C_0'V_{m-s}^*(z) - \frac{1}{2}\omega_{m-s}^2 L'C_m'^*(z)V_s(z), \tag{A.7b}$$

$$\frac{d^2V_{m+s}(z)}{dz^2} = -\omega_{m+s}^2 L'C_0'V_{m+s}(z) - \frac{1}{2}\omega_{m+s}^2 L'C_m'(z)V_s(z). \tag{A.7c}$$

Note that there are three additional equations which are the complex conjugate form of (A.7). Assuming all the signals are traveling in the same direction of the carrier, one has

$$V_s(z) = A_s(z)e^{-j\beta_s z}, \tag{A.8a}$$

$$V_{m-s}^*(z) = A_{m-s}^*(z)e^{j\beta_{m-s} z}, \tag{A.8b}$$

$$V_{m+s}(z) = A_{m+s}(z)e^{-j\beta_{m+s} z}. \tag{A.8c}$$

Suppose the transmission line is non-dispersive over all the interested frequencies, that is,

$$\frac{\omega_s}{\beta_s} = \frac{\omega_{m-s}}{\beta_{m-s}} = \frac{\omega_{m+s}}{\beta_{m+s}} = \frac{\omega_m}{\beta_m} = v_p = \frac{1}{\sqrt{L'C_0'}}, \tag{A.9}$$

which indicates that

$$\beta_{m\pm s} = \beta_m \pm \beta_s. \tag{A.10}$$

When the capacitance modulation index ξ is small, the amplitude terms $A(z)$ in (A.8) are slowly varying functions of z and the terms involving $d^2A(z)/dz^2$ may be neglected. Then

substituting (A.3), (A.4) and (A.8) into (A.7), we have

$$-2j\beta_s\frac{dA_s(z)}{dz}-\beta_s^2A_s(z)=-\omega_s^2L'C_0'A_s(z) \\ -\frac{1}{2}\omega_s^2L'C_0'\xi e^{j\phi_m}A_{m-s}^*(z)-\frac{1}{2}\omega_s^2L'C_0'\xi e^{-j\phi_m}A_{m+s}(z), \quad \text{(A.11a)}$$

$$2j\beta_{m-s}\frac{dA_{m-s}^*(z)}{dz}-\beta_{m-s}^2A_{m-s}^*(z)=-\omega_{m-s}^2L'C_0'A_{m-s}^*(z)-\frac{1}{2}\omega_{m-s}^2L'C_0'\xi e^{-j\phi_m}A_s(z), \quad \text{(A.11b)}$$

$$-2j\beta_{m+s}\frac{dA_{m+s}(z)}{dz}-\beta_{m+s}^2A_{m+s}(z)=-\omega_{m+s}^2L'C_0'A_{m+s}(z)-\frac{1}{2}\omega_{m+s}^2L'C_0'\xi e^{j\phi_m}A_s(z). \quad \text{(A.11c)}$$

Using the condition in (A.9) that $\beta^2=\omega^2L'C_0'$, the equations are reduced to

$$\frac{dA_s(z)}{dz}=-\frac{1}{4}j\beta_s\xi e^{j\phi_m}A_{m-s}^*(z)-\frac{1}{4}j\beta_s\xi e^{-j\phi_m}A_{m+s}(z), \quad \text{(A.12a)}$$

$$\frac{dA_{m-s}^*(z)}{dz}=\frac{1}{4}j\beta_{m-s}\xi e^{-j\phi_m}A_s(z), \quad \text{(A.12b)}$$

$$\frac{dA_{m+s}(z)}{dz}=-\frac{1}{4}j\beta_{m+s}\xi e^{j\phi_m}A_s(z). \quad \text{(A.12c)}$$

Combining the equations (A.12) with (A.10), we have

$$\frac{d^2A_s(z)}{dz^2}+\frac{1}{8}\xi^2\beta_s^2A_s(z)=0, \quad \text{(A.13)}$$

which has a general solution of

$$A_s(z)=c_1e^{\gamma z}+c_2e^{-\gamma z}, \quad \text{(A.14a)}$$

where

$$\gamma=j\frac{1}{2\sqrt{2}}\xi\beta_s, \quad \text{(A.14b)}$$

and c_1, c_2 are complex constants to be determined by the boundary conditions. Back to (A.12), we then also have

$$A_{m-s}^*(z)=\frac{1}{\sqrt{2}}\frac{\beta_{m-s}}{\beta_s}e^{-j\phi_m}\left(c_1e^{\gamma z}-c_2e^{-\gamma z}\right)+c_3e^{-j\phi_m}, \quad \text{(A.14c)}$$

$$A_{m+s}(z)=-\frac{1}{\sqrt{2}}\frac{\beta_{m+s}}{\beta_s}e^{j\phi_m}\left(c_1e^{\gamma z}-c_2e^{-\gamma z}\right)-c_3e^{j\phi_m}, \quad \text{(A.14d)}$$

where c_3 is another constant to be determined. Put (A.14) into (A.8) and then into (A.6). The boundary conditions are

$$v_s(0,t) = V_0\cos(\omega_s t + \phi_s) = \frac{1}{2}V_0 e^{j\phi_s}e^{j\omega_s t} + \frac{1}{2}V_0 e^{-j\phi_s}e^{-j\omega_s t}, \tag{A.15a}$$

$$v_{m-s}(0,t) = 0, \tag{A.15b}$$

$$v_{m+s}(0,t) = 0. \tag{A.15c}$$

The constants are thus determined as

$$c_1 = c_2 = \frac{1}{2}V_0 e^{j\phi_s}, \quad c_3 = 0. \tag{A.16}$$

Finally, the solution is obtained as

$$v_s(z,t) = V_0\cos\left(\frac{1}{2\sqrt{2}}\xi\beta_s z\right)\cos(\omega_s t - \beta_s z + \phi_s), \tag{A.17a}$$

$$v_{m-s}(z) = \frac{V_0}{\sqrt{2}}\frac{\beta_{m-s}}{\beta_s}\sin\left(\frac{1}{2\sqrt{2}}\xi\beta_s z\right)\sin(\omega_{m-s}t - \beta_{m-s}z + \phi_m - \phi_s), \tag{A.17b}$$

$$v_{m+s}(z) = \frac{V_0}{\sqrt{2}}\frac{\beta_{m+s}}{\beta_s}\sin\left(\frac{1}{2\sqrt{2}}\xi\beta_s z\right)\sin(\omega_{m+s}t - \beta_{m+s}z + \phi_m + \phi_s). \tag{A.17c}$$

One more comment is about the power relation. The average power associated with each tone is

$$P_s(z) = \frac{V_0^2}{2Z_0}\cos^2\left(\frac{1}{2\sqrt{2}}\xi\beta_s z\right), \tag{A.18a}$$

$$P_{m-s}(z) = \frac{V_0^2}{4Z_0}\left(\frac{\beta_{m-s}}{\beta_s}\right)^2\sin^2\left(\frac{1}{2\sqrt{2}}\xi\beta_s z\right), \tag{A.18b}$$

$$P_{m+s}(z) = \frac{V_0^2}{4Z_0}\left(\frac{\beta_{m+s}}{\beta_s}\right)^2\sin^2\left(\frac{1}{2\sqrt{2}}\xi\beta_s z\right), \tag{A.18c}$$

where $Z_0 = \sqrt{L'/C_0'}$ is the characteristic impedance of the transmission line. Given the input (A.15), whose power is

$$P_{in} = \frac{V_0^2}{2Z_0}, \tag{A.19}$$

the power change of the signal at the fundamental tone ω_s is $P_s - P_{in}$. The Manley-Rowe relation [49] is thus satisfied by examining the relation that

$$\frac{P_s - P_{in}}{\beta_s} - \frac{P_{m-s}}{\beta_{m-s}} + \frac{P_{m+s}}{\beta_{m+s}} = 0. \tag{A.20}$$

APPENDIX B

General Isolation of Dispersive DMC

It is assumed in Section 2.2.1 that DMC should best work in the nondispersion region. However, to fully utilize the bandwidth of the DMC as a periodic structure which has a low-pass feature, the upper-sideband output, where better gain can be achieved than the lower sideband, may be pushed close to the cutoff region of the DMC, where dispersion has to be considered. In this appendix, a more general isolation equation without assumption of the equal phase velocity assumed by (2.4) is provided.

The derivation generally follows the same procedure as described in Section 2.2.1, except some equations are rewritten to keep their original form without modification of their phase terms, especially. For instance, the carrier voltage in (2.7) should be rewritten as

$$v_m(z,t) = V_{m0}\cos(\omega_m t - \beta_m z + \phi_m) = \frac{1}{2}V_{m0}e^{j\phi_m}e^{j(\omega_m t-\beta_m z)} + \frac{1}{2}V_{m0}e^{-j\phi_m}e^{-j(\omega_m t-\beta_m z)}. \quad \text{(B.1)}$$

The phase constant β_m is kept in the phase terms. Consequently, the complex-valued capacitance modulation, defined in (2.10) and denoted by (2.9), now becomes

$$C_i(t) = C_1 V_{m0}e^{j\phi_m}e^{j(\omega_m t-\beta_m i\Delta z)}, \quad i = 1, 2, ..., N. \quad \text{(B.2)}$$

Similarly, the complex-valued received and transmitted signals, initially as (2.13) and (2.14), are rewritten as

$$V^{\mathrm{RX}}(z,t) = V_0 e^{j\phi_s^{\mathrm{RX}}}e^{j(\omega_s t-\beta_s z)}, \quad \text{(B.3)}$$

$$V^{\mathrm{TX}}(z,t) = V_0 e^{j\phi_s^{\mathrm{TX}}}e^{j(\omega_s t+\beta_s z)}. \quad \text{(B.4)}$$

For received signal, the complex-valued, excited up-converted voltage at ith capacitor is

now changed from (2.17) to be

$$V_{i,m\pm s}^{\mathrm{RX}}(t) = -j \cdot g_{c,m\pm s} V_0 e^{j(\phi_m \pm \phi_s^{\mathrm{RX}})} \cdot e^{j(\omega_m \pm \omega_s)t} e^{-j(\beta_m \pm \beta_s) i\Delta z}, \tag{B.5}$$

where $g_{c,m\pm s}$ are the same conversion gains as defined in (2.18). Then, the summed-up excited voltage at the transceiver end becomes

$$\begin{aligned} V_{\mathrm{transceiver},m\pm s}^{\mathrm{RX}}(t) &= \sum_{i=1}^{N} V_{i,m\pm s}^{\mathrm{RX}} \left[t - \frac{\beta_{m\pm s}(N-i)\Delta z}{\omega_m \pm \omega_s} \right] \\ &= -j \cdot g_{c,m\pm s} V_0 e^{j(\phi_m \pm \phi_s^{\mathrm{RX}})} \sum_{i=1}^{N} e^{j(\omega_m \pm \omega_s)t} e^{-j\beta_{m\pm s}(N-i)\Delta z} e^{-j(\beta_m \pm \beta_s) i\Delta z} \\ &= -j \cdot g_{c,m\pm s} V_0 e^{j(\phi_m \pm \phi_s^{\mathrm{RX}})} \cdot e^{j(\omega_m \pm \omega_s)t} e^{-j\beta_{m\pm s} N\Delta z} \sum_{i=1}^{N} e^{j[\beta_{m\pm s} - (\beta_m \pm \beta_s)] i\Delta z}, \end{aligned} \tag{B.6}$$

where $\beta_{m\pm s}$ represent the phase constants at $\omega_m \pm \omega_s$, which are not necessarily equal to $\beta_m \pm \beta_s$, unless the phase velocities are equal as assumed in (2.4) and then (B.6) is reduced to (2.19). Similarly, for transmitted signal, we have

$$V_{i,m\pm s}^{\mathrm{TX}}(t) = -j \cdot g_{c,m\pm s} V_0 e^{j(\phi_m \pm \phi_s^{\mathrm{TX}})} \cdot e^{j(\omega_m \pm \omega_s)t} e^{-j(\beta_m \mp \beta_s) i\Delta z}, \tag{B.7}$$

and then

$$\begin{aligned} V_{\mathrm{transceiver},m\pm s}^{\mathrm{TX}}(t) &= \sum_{i=1}^{N} V_{i,m\pm s}^{\mathrm{TX}} \left[t - \frac{\beta_{m\pm s}(N-i)\Delta z}{\omega_m \pm \omega_s} \right] \\ &= -j \cdot g_{c,m\pm s} V_0 e^{j(\phi_m \pm \phi_s^{\mathrm{TX}})} \sum_{i=1}^{N} e^{j(\omega_m \pm \omega_s)t} e^{-j\beta_{m\pm s}(N-i)\Delta z} e^{-j(\beta_m \mp \beta_s) i\Delta z} \\ &= -j \cdot g_{c,m\pm s} V_0 e^{j(\phi_m \pm \phi_s^{\mathrm{TX}})} \cdot e^{j(\omega_m \pm \omega_s)t} e^{-j\beta_{m\pm s} N\Delta z} \sum_{i=1}^{N} e^{j[\beta_{m\pm s} - (\beta_m \mp \beta_s)] i\Delta z}. \end{aligned} \tag{B.8}$$

Consequently, the isolation is formulated as

$$\mathrm{ISO}_{m\pm s} = \left| \frac{V_{\mathrm{transceiver},m\pm s}^{\mathrm{TX}}}{V_{\mathrm{transceiver},m\pm s}^{\mathrm{RX}}} \right| = \left| \frac{\sum_{i=1}^{N} e^{j[\beta_{m\pm s} - (\beta_m \pm \beta_s)] i\Delta z}}{\sum_{i=1}^{N} e^{j[\beta_{m\pm s} - (\beta_m \mp \beta_s)] i\Delta z}} \right|. \tag{B.9}$$

In the special case where the DMC works in the nondispersive region and thus $\beta_{m\pm s} = \beta_m \pm \beta_s$, (B.9) is reduced to (2.25).

The minor imperfection in the DMC, as discussed in this section, can provide additional insight of treating the isolation of the DMC as a gross contribution of the individual varactors in the DMC as capacitive mixers.

References

[1] C. E. Shannon and W. Weaver, *The Mathematical Theory of Communication*, 1st ed. Champaign, IL, USA: Univ. of Illinois Press, 1949.

[2] A. Goldsmith, *Wireless Communications*, 1st ed. Cambridge, UK: Cambridge Univ. Press, 2005.

[3] D. W. Bliss, P. A. Parker, and A. R. Margetts, "Simultaneous transmission and reception for improved wireless network performance," in *Proc. IEEE Statist. Signal Process. Workshop*, Madison, WI, USA, Aug. 2007, pp. 478–482.

[4] J. I. Choi, M. Jain, K. Srinivasan, P. Levis, and S. Katti, "Achieving single channel, full duplex wireless communication," in *Proc. ACM MobiCom*, Chicago, IL, USA, Sep. 2010, pp. 1–12.

[5] M. Duarte, C. Dick, and A. Sabharwal, "Experiment-driven characterization of full-duplex wireless systems," *IEEE Trans. Wireless Commun.*, vol. 11, no. 12, pp. 4296–4307, Dec. 2012.

[6] M. E. Knox, "Single antenna full duplex communications using a common carrier," in *Proc. 13th Annu. IEEE Wireless Microw. Technol. Conf.*, Cocoa Beach, FL, USA, Apr. 2012, pp. 1–6.

[7] D. Bharadia, E. McMilin, and S. Katti, "Full duplex radios," in *Proc. ACM SIGCOMM*, Hong Kong, China, Aug. 2013, pp. 375–386.

[8] A. Sabharwal, P. Schniter, D. Guo, D. W. Bliss, S. Rangarajan, and R. Wichman, "In-band full-duplex wireless: Challenges and opportunities," *IEEE J. Sel. Areas Commun.*, vol. 32, no. 9, pp. 1637–1652, Sep. 2014.

[9] D. M. Pozar, *Microwave Engineering*, 3rd ed. New York, NY, USA: Wiley, 2005.

[10] H. Bosma, "On stripline Y-circulation at UHF," *IEEE Trans. Microw. Theory Techn.*, vol. 12, no. 1, pp. 61–72, Jan. 1964.

[11] J. Adam, L. Davis, G. Dionne, E. Schloemann, and S. Stizer, "Ferrite devices and materials," *IEEE Trans. Microw. Theory Techn.*, vol. 50, no. 3, pp. 721–737, Mar. 2002.

[12] A. Geiler and V. Harris, "Atom magnetism: Ferrite circulators – Past, present, and future," *IEEE Microw. Mag.*, vol. 15, no. 6, pp. 66–72, Sep.-Oct. 2014.

[13] S. Tanaka, N. Shimomura, and K. Ohtake, "Active circulators – The realization of circulators using transistors," *Proc. IEEE*, vol. 53, no. 3, pp. 260–267, Mar. 1965.

[14] M. A. Smith, "GaAs monolithic implementation of active circulators," in *IEEE MTT-S Int. Microwave Symp. Dig.*, New York, NY, USA, May 1988, pp. 1015–1016.

[15] S. Hara, T. Tokumitsu, and M. Aikawa, "Novel unilateral circuits for MMIC circulators," *IEEE Trans. Microw. Theory Techn.*, vol. 38, no. 10, pp. 1399–1406, Oct. 1990.

[16] S. K. Cheung, T. Halloran, W. Weedon, and C. Caldwell, "MMIC-based quadrature hybrid quasi-circulators for simultaneous transmit and receive," *IEEE Trans. Microw. Theory Techn.*, vol. 58, no. 3, pp. 489–497, Mar. 2010.

[17] T. Kodera, D. L. Sounas, and C. Caloz, "Magnetless nonreciprocal metamaterial (MNM) technology: Application to microwave components," *IEEE Trans. Microw. Theory Techn.*, vol. 61, no. 3, pp. 1030–1042, Mar. 2013.

[18] S. Furukawa and S. Horiguchi, "The noise performance of the active circulator," *Proc. IEEE*, vol. 55, no. 11, pp. 2048–2050, Nov. 1967.

[19] A. Gasmi, B. Huyart, E. Bergeault, and L. Jallet, "Noise and power optimization of a MMIC quasi-circulator," *IEEE Trans. Microw. Theory Techn.*, vol. 45, no. 9, pp. 1572–1577, Sep. 1997.

[20] G. Carchon and B. Nauwelaers, "Power and noise limitations of active circulators," *IEEE Trans. Microw. Theory Techn.*, vol. 48, no. 2, pp. 316–319, Feb. 2000.

[21] Z. Yu and S. Fan, "Complete optical isolation created by indirect interband photonic transitions," *Nat. Photon.*, vol. 3, pp. 91–94, Feb. 2009.

[22] L. D. Tzuang, K. Fang, P. Nussenzveig, S. Fan, and M. Lipson, "Non-reciprocal phase shift induced by an effective magnetic flux for light," *Nat. Photon.*, vol. 8, pp. 701–705, Sep. 2014.

[23] C. H. Cox and E. I. Ackerman, "TIPRx: A transmit-isolating photonic receiver," *J. Lightw. Technol.*, vol. 32, no. 20, pp. 3630–3636, Oct. 2014.

[24] D. L. Sounas, C. Caloz, and A. Alu, "Giant non-reciprocity at the subwavelength scale using angular momentum-biased metamaterials," *Nat. Commun.*, vol. 4, Sep. 2013, Art. ID 2407.

[25] N. A. Estep, D. L. Sounas, J. Soric, and A. Alu, "Magnetic-free non-reciprocity and isolation based on parametrically modulated coupled-resonator loops," *Nature Phys.*, vol. 10, pp. 923–927, Dec. 2014.

[26] N. A. Estep, D. L. Sounas, and A. Alu, "Magnetless microwave circulators based on spatiotemporally modulated rings of coupled resonators," *IEEE Trans. Microw. Theory Techn.*, vol. 64, no. 2, pp. 502–518, Feb. 2016.

[27] N. Reiskarimian and H. Krishnaswamy, "Magnetic-free non-reciprocity based on staggered commutation," *Nat. Commun.*, vol. 7, Apr. 2016, Art. ID 11217.

[28] Y. E. Wang, "Non-reciprocity with time-varying transmission lines (TVTLs)," in *IEEE Int. Wireless Inform. Technol. Syst. Conf.*, Maui, HI, USA, Nov. 2012, pp. 1–4.

[29] S. Qin and Y. E. Wang, "Parametric conversion with distributedly modulated capacitors (DMC) for low-noise and non-reciprocal RF front-ends," in *IEEE MTT-S Int. Microwave Symp. Dig.*, Seattle, WA, USA, Jun. 2013, pp. 1–3.

[30] Y. E. Wang, "Time-varying transmission lines (TVTL) – A new pathway to non-reciprocal and intelligent RF front-ends," in *Proc. IEEE Radio Wireless Symp.*, Newport Beach, CA, USA, Jan. 2014, pp. 148–150.

[31] S. Qin, Q. Xu, and Y. E. Wang, "Nonreciprocal components with distributedly modulated capacitors," *IEEE Trans. Microw. Theory Techn.*, vol. 62, no. 10, pp. 2260–2272, Oct. 2014.

[32] S. Qin and Y. E. Wang, "Broadband parametric circulator with balanced monolithic integrated distributedly modulated capacitors (DMC)," in *IEEE MTT-S Int. Microwave Symp. Dig.*, San Francisco, CA, USA, May 2016, pp. 1–4.

[33] A. Kamal, J. Clarke, and M. H. Devoret, "Noiseless non-reciprocity in a parametric active device," *Nature Phys.*, vol. 7, pp. 311–315, Apr. 2011.

[34] A. L. Cullen, "A travelling-wave parametric amplifier," *Nature*, vol. 181, p. 332, Feb. 1958.

[35] P. K. Tien and H. Suhl, "A traveling-wave ferromagnetic amplifier," *Proc. IEEE*, vol. 46, no. 4, pp. 700–706, Apr. 1958.

[36] P. K. Tien, "Parametric amplification and frequency mixing in propagating circuits," *J. Appl. Phys.*, vol. 29, no. 9, pp. 1347–1357, Sep. 1958.

[37] R. Landauer, "Parametric amplification along nonlinear transmission line," *J. Appl. Phys.*, vol. 31, no. 3, pp. 479–484, Mar. 1960.

[38] D. Jager and F.-J. Tegude, "Nonlinear wave propagation along periodic-loaded transmission line," *J. Appl. Phys.*, vol. 15, no. 4, pp. 393–397, Apr. 1978.

[39] A. Suarez and R. Melville, "Simulation-assisted design and analysis of varactor-based frequency multipliers and dividers," *IEEE Trans. Microw. Theory Techn.*, vol. 54, no. 3, pp. 1166–1179, Mar. 2006.

[40] B. Gray, B. Melville, and J. S. Kenney, "Analytical modeling of microwave parametric upconverters," *IEEE Trans. Microw. Theory Techn.*, vol. 58, no. 8, pp. 2118–2124, Aug. 2010.

[41] S. Magierowski, J.-F. Bousquet, Z. Zhao, and T. Zourntos, "RF CMOS parametric downconverters," *IEEE Trans. Microw. Theory Techn.*, vol. 58, no. 3, pp. 518–528, Mar. 2010.

[42] S. Kabir, S. Magierowski, G. G. Messier, and Z. Zhao, "A direct 100 ghz parametric CMOS tripler," *IEEE Microw. Wireless Compon. Lett.*, vol. 23, no. 10, pp. 557–559, Oct. 2013.

[43] W. Lee and E. Afshari, "Distributed parametric resonator: A passive CMOS frequency divider," *IEEE J. Solid-State Circuits*, vol. 45, no. 9, pp. 1834–1844, Sep. 2010.

[44] ——, "Low-noise parametric resonant amplifier," *IEEE Trans. Circuits Syst. I, Reg. Papers*, vol. 58, no. 3, pp. 479–492, Mar. 2011.

[45] ——, "A CMOS noise-squeezing amplifier," *IEEE Trans. Microw. Theory Techn.*, vol. 60, no. 2, pp. 329–339, Feb. 2012.

[46] H. R. Mohebbi and A. H. Majedi, "Analysis of series-connected discrete Josephson transmission line," *IEEE Trans. Microw. Theory Techn.*, vol. 57, no. 8, pp. 1865–1873, Aug. 2009.

[47] O. Yaakobi, L. Friedland, C. Macklin, and I. Siddiqi, "Parametric amplification in Josephson junction embedded transmission lines," *Phys. Rev. B, Condens. Matter*, vol. 87, no. 14, Apr. 2013, Art. ID 144301.

[48] A. V. der Ziel, "On the mixing properties of nonlinear condensers," *J. Appl. Phys.*, vol. 19, no. 11, pp. 999–1006, Nov. 1948.

[49] J. M. Manley and H. E. Rowe, "Some general properties of nonlinear elements – Part I. General energy relations," *Proc. IRE*, vol. 44, no. 7, pp. 904–913, Jul. 1956.

[50] H. E. Rowe, "Some general properties of nonlinear elements – Part II. Small signal theory," *Proc. IRE*, vol. 46, no. 5, pp. 850–860, May 1958.

[51] C. L. Dolph, "A current distribution for broadside arrays which optimizes the relationship between beam width and side-lobe level," *Proc. IRE*, vol. 34, no. 6, pp. 335–348, Jun. 1946.

[52] MA46580-1209 – M/A-COM Technology Solutions. [Online]. Available: http://www.macomtech.com/datasheets/MA46580_MA46585.pdf

[53] E. A. Etellisi, M. A. Elmansouri, and D. S. Filipovic, "Wideband monostatic simultaneous transmit and receive (STAR) antenna," *IEEE Trans. Antennas Propag.*, vol. 64, no. 1, pp. 6–15, Jan. 2016.